**Rewired m6A methylation of promoter antisense RNAs in Alzheimer's disease regulates global gene transcription in the 3D nucleome**

Benxia Hu[1,#], Yuqiang Shi[1,#], Feng Xiong[1], Yi-Ting Chen[1,2], Xiaoyu Zhu[1], Elisa Carrillo [1], Xingzhao Wen[3,4], Nathan Drolet[1], Chetan Rajpurohit[5], Xiangmin Xu[6,7], Dung-Fang Lee[2,8], Claudio Soto[2,9], Sheng Zhong[3,4], Vasanthi Jayaraman [1,2], Hui Zheng[5], Wenbo Li[1,2] *

[1] Department of Biochemistry and Molecular Biology, McGovern Medical School, University of Texas Health Science Center, Houston, TX, USA.

[2] The University of Texas MD Anderson Cancer Center and UTHealth Houston Graduate School of Biomedical Sciences, Houston, TX, USA.

[3] Program in Bioinformatics and Systems Biology, University of California San Diego, La Jolla, CA, USA.

[4] Shu Chien-Gene Lay Department of Bioengineering, University of California San Diego, La Jolla, CA, USA.

[5] Huffington Center on Aging, Baylor College of Medicine, Houston, Texas, USA.

[6] Department of Anatomy and Neurobiology, School of Medicine, University of California, Irvine, CA, USA.

[7] Center for Neural Circuit Mapping (CNCM), University of California, Irvine, CA, USA.

[8] Department of Integrative Biology and Pharmacology, McGovern Medical School, The University of Texas Health Science Center at Houston, Houston, TX, USA.

[9] Department of Neurology, McGovern Medical School, University of Texas Health Science Center, Houston, TX, USA.

[#] Contributed equally.

[*] Corresponding author, Wenbo.li@uth.tmc.edu.

**Abstract**

$N^6$-methyladenosine (m6A) is the most prevalent internal RNA modification that can impact mRNA expression post-transcriptionally. Recent progress indicates that m6A also acts on nuclear or chromatin-associated RNAs to impact transcriptional and epigenetic processes. However, the landscapes and functional roles of m6A in human brains and neurodegenerative diseases, including Alzheimer's disease (AD), have been under-explored. Here, we examined RNA m6A methylome using total RNA-seq and meRIP-seq in middle frontal cortex tissues of post-mortem human brains from individuals with AD and age-matched counterparts. Our results revealed AD-associated alteration of m6A methylation on both mRNAs and various noncoding RNAs. Notably, a series of promoter antisense RNAs (paRNAs) displayed cell-type-specific expression and changes in AD, including one produced adjacent to the *MAPT* locus that encodes the Tau protein. We found that *MAPT-paRNA* is enriched in neurons, and m6A positively controls its expression. In iPSC-derived human excitatory neurons, *MAPT-paRNA* promotes expression of hundreds of genes related to neuronal and synaptic functions, including a key AD resilience gene *MEF2C*, and plays a neuroprotective role against excitotoxicity. By examining RNA-DNA interactome in the three-dimensional (3D) nuclei of human brains, we demonstrated that brain paRNAs can interact with both *cis*- and *trans*-chromosomal target genes to impact their transcription. These data together reveal previously unexplored landscapes and functions of noncoding RNAs and m6A methylome in brain gene regulation, neuronal survival and AD pathogenesis.

**Introduction**

Alzheimer's disease (AD) is the most common cause of dementia (60–70% of all cases), and affects 5% of the population over 60 years (or approximately 1% of the total population)[1]. AD is pathologically characterized by massive neuronal loss, the presence of amyloid-beta (Aβ) plaques, and Tau neurofibrillary tangles (NFTs) in the brain[2,3]. Despite extensive studies of AD, there are still limited therapeutic options that can effectively treat this devastating disease. Identifying new molecular players in AD pathogenesis is important to offer further insights and potential targets for combating this disease.

In the past decade, studies of RNA chemical modifications have founded a field that is referred to as "epitranscriptomics"[4,5]. Among these RNA modifications, N[6]-methyladenosine (m6A) is the most abundant internal RNA methylation in mammalian cells, and it can impact mRNA stability, trafficking, and translation[4,5]. Analogous to the mechanism of epigenetics, biological functions of m6A are considered to be mediated by specific proteins that write, read, and erase this mark, which are referred to as m6A writers (e.g., METTL3), readers (e.g., YTH proteins), and erasers (e.g., FTO and ALKBH5), respectively[4,5]. In addition to post-transcriptional roles on mRNAs, m6A methylation is increasingly realized to bear transcriptional roles by modifying nuclear or chromatin-associated RNAs to control gene transcription via functionally cross-talking to epigenetic processes[6-10]. Examples include m6A regulation of *Xist* lncRNA[8,11], retrotransposon RNAs[10,12-14], or enhancer RNAs[7,15]. These results have provided a new perspective to study the roles of m6A in gene regulation in development and diseases, which encompasses both transcriptional and post-transcriptional processes. Interestingly, m6A methylation seems to play unique functions in the brain. For example, in both mice and human brains, m6A landscapes display a pattern distinctive from other tissues[16]. In murine models, conditional depletion of genes encoding a component of the m6A methyltransferase complex, Mettl14, or a cytoplasmic m6A reader protein, Ythdf1, severely affected neurogenesis and cognitive functions[17,18]. However, despite efforts[19], the landscapes and functional roles of m6A or other epitranscriptomic modifications in human brains and AD remain minimally explored.

Regulatory long noncoding RNAs (lncRNAs) are pervasively produced in the human genome[20,21]. A large fraction of these transcripts originate from divergent transcription at

3

80    promoters of active protein-coding genes (>60% in human ESCs[22]), which are interchangeably

81    referred to as promoter antisense RNAs (paRNAs) or PTOMPTs[23-27]. Some studies reported that

82    paRNAs can regulate the expression of mRNAs divergently produced from the same

83    promoters[27,28]. Actually, deregulation of lncRNAs has been long observed in AD[29-31]. An early

84    example is an antisense RNA produced within the *BACE1* gene locus that was proposed to

85    regulate *BACE1* expression to impact AD disease progression[32]. High resolution transcriptomes

86    in AD brains have now permitted rapid discovery of enormous ncRNAs[30,31]. A recent work

87    suggested that AD-associated natural antisense transcripts (NAT), some of which are paRNAs,

88    can play roles in the translational control of crucial disease proteins including MAPT/Tau to

89    impact AD pathogenesis[33]. However, another study reported inconsistent results[34]. These studies

90    together indicated that the roles of lncRNAs are still under-studied in human AD brains, and

91    their mechanisms of action are poorly understood.

92

93    Here, we characterized RNA m6A methylome from individuals diagnosed with AD and from

94    cognitively normal age-matched individuals. We uncovered a large number of m6A-modified

95    RNAs in the human brain, including both mRNAs and ncRNAs, many of which were previously

96    unannotated. RNA m6A methylome in AD brains displays alteration as compared to controls,

97    and there is positive correlation between its signals and expression levels of mRNA and

98    ncRNAs. Subsequently, we focused on paRNAs and used induced pluripotent stem cell (iPSC)-

99    derived human excitatory neurons (i3Neurons) to functionally investigate regulatory roles of an

100    m6A-modified *MAPT-paRNA* transcribed next to *MAPT*, a key AD-associated disease locus. Our

101    data revealed that *MAPT-paRNA* shows neuron-preferred expression and is upregulated in AD. It

102    promotes the expression of many neuronal and synaptic genes via navigating the three-

103    dimensional (3D) genome organization, which is required for neuronal survival under excitotoxic

104    conditions. This work unraveled previously unexplored landscapes and the role of chemical

105    modification on AD-associated ncRNAs, linking epitranscriptome to gene transcriptional control

106    in the 3D genome and AD pathogenesis.

107

108    **Results**

109    **The transcriptome and m6A epitranscriptome of human AD brains on coding and**

110    **noncoding RNAs**

111    From a cohort of individuals diagnosed with sporadic AD (n = 6; mean age = 66) and from

112    cognitively normal age-matched counterparts (n = 6; mean age = 65, hereafter referred to as

113    Normal), we collected the middle frontal cortex tissue (mFC), a region pathologically affected in

114    AD[35]. Subsequent to autopsy, neuropathologic examination revealed high levels of

115    phosphorylated Tau neurofibrillary tangles and amyloid-β burden (**Supplementary Table 1**).

116    We analyzed the transcriptome by strand-specific ribo-depleted total RNA-seq, with the aim of

117    examining both mRNAs and various ncRNAs. RNA m6A methylome was examined by m6A

118    antibody-based immunoprecipitation (MeRIP-seq) (**see methods**). A summary of our sequencing

119    datasets can be found in **Supplementary Table 2**.

120

121    Analysis of total RNA-seq data identified 416 and 519 genes significantly upregulated and

122    downregulated in AD as compared to Normal groups, respectively (**Supplementary Fig. 1A**,

123    gene lists in **Supplementary Table 3**). These changes are consistent with a previous study that

124    conducted total RNA-seq in the lateral temporal lobe (LTL) region of AD/Normal human

125    brains[36] (**Supplementary Fig. 1B,C**). Gene Ontology (GO) analysis of differentially expressed

126    genes (DEGs) showed that AD-upregulated genes are related to development, while the AD-

127    downregulated genes are enriched in neuronal/synaptic functions (**Supplementary Fig. 1D,E,**

128    and **Supplementary Table 4**). This is in accord with the knowledge that neuronal/synaptic genes

129    are reduced in AD[37]. This also suggests that tissue-level gene deregulation that we found here

130    largely reflects changes in neurons[38]. Several representative examples of deregulated genes are

131    shown in **Supplementary Fig. 1F**. *YAP1*, a gene encoding a key transcription regulator, was

132    induced in AD, whereas AD-downregulated genes are exemplified by neuronal transcriptional

133    factor gene *NEUROD6* and those encoding glutamate decarboxylases essential for inhibitory

134    neurotransmitter gamma-aminobutyric acid (GABA) synthesis, e.g., *GAD1*/*GAD2*
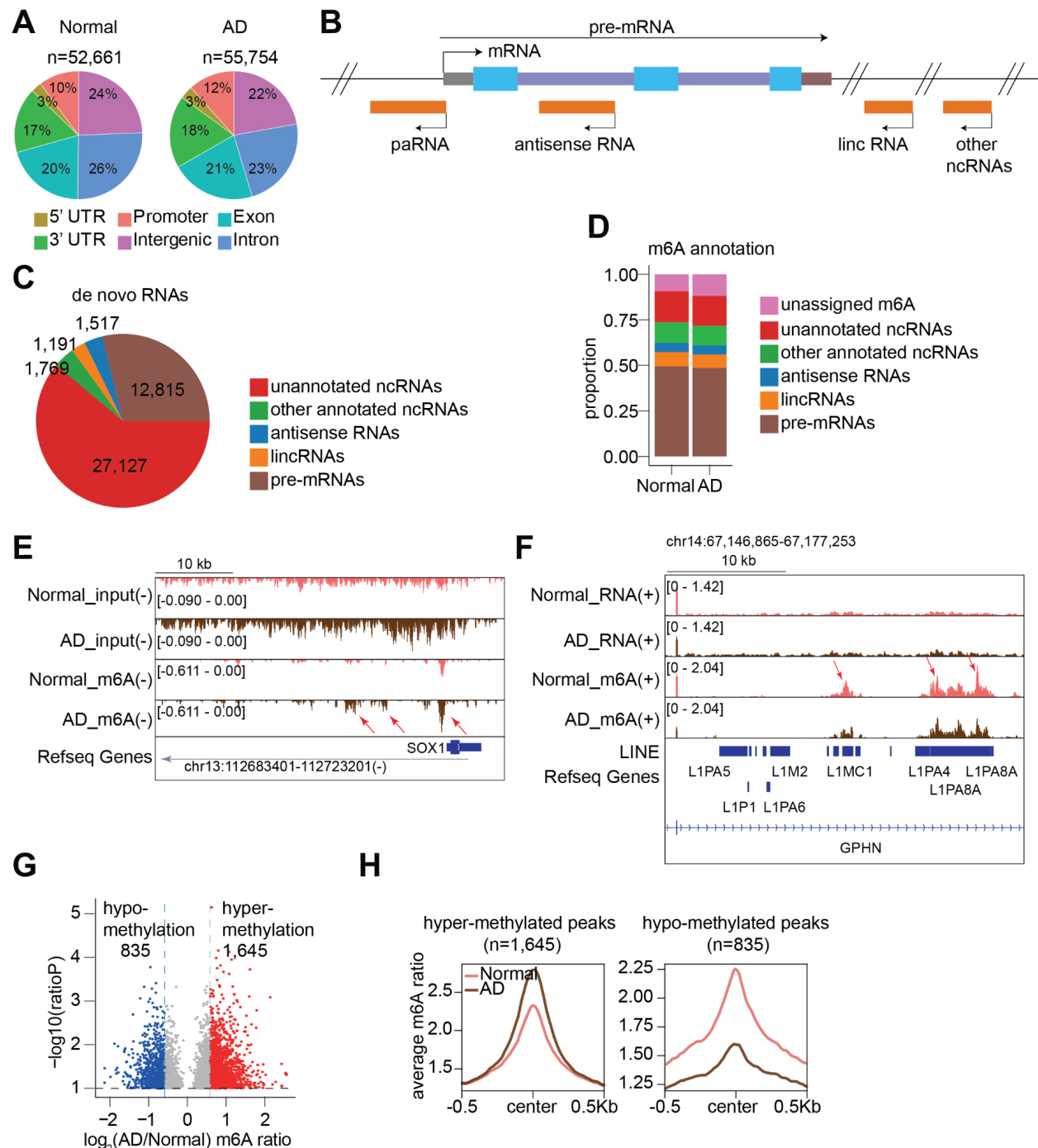
135    (**Supplementary Fig. 1F**).

**Figure 1. m6A methylome on coding and noncoding RNAs in the mFC regions of human brains.**
**A**. Piecharts showing the m6A peak distribution based on genomic locations in post-mortem human mFC tissues from Normal and AD donors, respectively. **B**. A model illustrating major categories of *de novo* identified transcripts, including pre-mRNAs and ncRNAs. **C**. A piechart showing the numbers of transcripts identified by the de novo calling. **D**. A barplot showing the assignment of m6A peaks to various *de novo* called transcripts. **E**. Genome browser tracks showing an example of ncRNA (a promoter antisense RNA from the *SOX1* locus) having m6A peaks in human Normal and AD brains. Input and m6A represent the average signals of RNA-seq and meRIP-seq datasets in this work, respectively. The arrows indicate m6A peaks. **F.** Similar to E, example tracks showing intronic L1 elements overlap m6A peaks in the intron of *GPHN* gene. (+) and (-) indicate the Watson and Crick strands, respectively. **G.** A volcano plot showing differential m6A peaks between Normal and AD brains. Red and blue dots

147 represent hyper- and hypo-methylated m6A sites in AD. **H**. Metaplots showing the aggregated m6A ratios of hyper-
148 and hypo-methylated m6A sites.
149

150 To examine the changes of RNA m6A methylome in AD versus Normal brains, we called strand-

151 specific m6A peaks on total RNA-Seq/MeRIP-seq datasets using MACS3[39,40], and identified

152 approximately 52,661 and 55,754 m6A peaks in Normal and AD mFC tissues, respectively

153 (**Supplementary Table 5**). A majority of peaks locate in the non-protein-coding portions of the

154 genome, i.e., around 60% were in intergenic regions, introns or promoter upstream regions (-2kb

155 to transcription start sites) (**Fig. 1A**). The remaining peaks overlapped with protein-coding

156 mRNA sequences (CDSs), and 5' or 3' untranslated regions (UTRs) (**Fig. 1A**). This is consistent

157 with the higher sensitivity of ribo-depletion strategy in RNA-seq to detect various ncRNAs. We

158 compared the features of m6A peaks in Normal and AD conditions, and found them to be overall

159 similar: they enrich the canonical RRACH motif, bearing comparable peak length (Normal:

160 236bp v.s. AD: 227bp) and average GC contents (0.47 v.s. 0.45) (**Supplementary Fig. 2A,B,C**).

161 The genomic distribution of m6A signals is quite similar between RNAs from Normal and AD

162 brains, too (**Supplementary Fig. 2D**). These results indicate that AD elicits a quantitative

163 rewiring of the RNA m6A landscape in the human brain, at least in the mFC region.

164

165 A large number of m6A peaks locating in the noncoding regions is consistent with recent work

166 about m6A on regulatory ncRNAs[7,8,12,15,41]. Annotation of m6A peaks using genomic locations is

167 not sufficient to precisely associate them to specific noncoding RNA transcripts (**Fig. 1A,B**). We

168 therefore need to first define a complete catalog of transcripts and their genomic coordinates in

169 the human brain by a *de novo* transcript calling method based on Hidden Markov Model (HMM)

170 [42,43]. Of the *de novo* identified transcripts, 12,815 overlap protein-coding genes and are thus

171 defined as pre-mRNAs in this work (**Fig. 1B,C**). There are 31,604 ncRNA transcripts in the

172 human brain (**Fig. 1C**), including 27,127 previously unannotated RNAs in the human

173 transcriptome. Of the remaining, 1,191 overlap annotated lncRNAs, 1,517 overlap annotated

174 antisense RNAs, and 1,769 overlap other annotated RNAs (snoRNAs, snRNAs, pseudo genes) in

175 gencode v19 (**Fig. 1C**). Approximately 90% of all m6A peaks can be assigned to these various

176 *de novo* identified RNAs (**Supplementary Fig. 2E,** and **Fig. 1D**). The ~10% unassigned peaks

177 are largely due to the fact that some RNAs are not identified as independent transcripts by the *de*

178 *novo* calling algorithm and thus m6A peaks on them are not assigned. As an example, of the

179     27,127 previously unannotated transcripts (**Fig. 1C,D**), an antisense RNA generated from the

180     *SOX1* gene promoter shows prominent m6A peaks (**Fig. 1E**). About 50% of m6A peaks were

181     assigned to the sense strand of pre-mRNAs, including exons, introns, 5'UTR and 3'UTR (**Fig.**

182     **1D,F**). Among these, interestingly, over ten-thousand peaks appear in introns and often overlap

183     transposable elements, in particular, intronic L1 elements (**Fig. 1F,** and **Supplementary Fig.**

184     **2F,G,H**). This is reminiscent of our previous work showing that many intronic L1 RNAs bear

185     high m6A methylation and play roles in gene transcriptional control[12]. Collectively, at the

186     transcriptome level, 60-70% of all m6A peaks are located in ncRNAs or introns as opposed to

187     mRNA regions (UTRs and exons), and the distribution pattern is largely similar in AD versus

188     Normal (**Supplementary Fig. 2H**). These results provided a comprehensive m6A RNA

189     methylome on mRNAs and ncRNAs in human Normal and AD brains, serving as a foundation to

190     study the functions of these m6A signals in gene expression regulation and AD biology.

191

192     **The alteration of m6A epitranscriptome in the human AD brains**

193     By calculating differential m6A methylation (**see methods**), we identified 835 and 1,645

194     differential m6A peaks (DMPs) showing hypo- and hyper-m6A-methylation in AD, respectively

195     (**Fig. 1G**). Here we defined m6A methylation levels as m6A ratios, the signal division between

196     meRIP-seq and RNA-seq in each peak. The changes in m6A ratios at the differential peaks can

197     be seen by meta-analysis (**Fig. 1H**), and the motifs in these regions remain canonical RRACH

198     (**Supplementary Fig. 3A**). A breakdown shows that DMPs overall occurred proportionally to

199     the total peak distribution, with about 40% of DMPs on pre-mRNAs (including exons, UTRs and

200     introns) and the other ~60% of DMPs are observed to be from ncRNAs (**Fig. 1D**, and

201     **Supplementary Fig. 3B**).

202

203     Previous m6A studies have shown correlation between changes of m6A and mRNA expression

204     levels[4,44]. We examined their correlation in AD brains by examining mRNAs bearing DMPs on

205     their exons or UTRs. By cumulative fraction analysis, we observed a positive correlation

206     between the two, i.e., m6A hyper-methylation is associated with mRNA expression increase in

207     AD, whereas hypo-methylation is associated with decrease (**Supplementary Fig. 3C,D**).

208     Interestingly, GO enrichment analyses of genes whose mRNAs display hyper-methylation show

209     terms related to transcriptional activities, whereas gene mRNAs with hypo-methylated peaks are

210    more relevant to synapse regulation (**Supplementary Fig. 3E,F**). Because of the known

211    expression reduction of synapse related genes in AD[37], this result suggests that hypo-methylation

212    of their mRNAs is associated with expression reduction during AD pathogenesis. We showed

213    two representative examples of m6A peaks in the 3'UTR regions that were hyper- or hypo-

214    methylated in AD compared to Normal, which correlates with their respective mRNA expression

215    changes (**Supplementary Fig. 3G,H**). We conducted similar analysis for ncRNAs, and observed

216    that m6A changes are also positively correlated with ncRNA expression alteration in AD, i.e.,

217    hyper-methylation is associated with ncRNA expression increase, whereas hypo-methylation

218    with decrease (**Supplementary Fig. 4A,B**). We show two representative examples of ncRNA

219    regions that were increased or decreased in AD compared to Normal, respectively

220    (**Supplementary Fig. 4C,D**).

221

222    **Identification and alteration of promoter antisense RNAs in AD brains**

223    We sought to focus on previously under-studied ncRNAs and their m6A modification in AD.

224    Visual inspection revealed a large number of paRNAs that display m6A peaks, which

225    interestingly include many produced from important neuronal and synaptic gene loci. For

226    example, an m6A-marked paRNA spanning ~18kb is generated from the *GRIN2A* locus (**Fig.**

227    **2A**), which codes for an important neurotransmitter receptor Glutamate Ionotropic Receptor

228    NMDA Type Subunit 2A. Similarly, another m6A-marked paRNA is produced antisense to the

229    promoter of *MAPT*, one of the most significant AD-associated loci as it encodes the Tau protein

230    (**Fig. 2B**). Importantly, functions of paRNAs have been minimally studied or understood in brain

231    gene regulation and AD biology. *De novo* calling identified 3,038 paRNAs in mFC brain regions

232    and about 37-39% of them display a m6A peak in either Normal or AD brains (**Supplementary**

233    **Fig. 5A**). GO term analysis showed that genes neighboring m6A-marked paRNAs are associated

234    with neuronal and synapse functions, which are deregulated processes in AD (**Fig. 2C,D**). In

235    comparison, mRNAs with m6A do not show such association (**Supplementary Fig. 5B**),

236    suggesting that m6A-marked paRNAs in mFCs may have specific relevance to neuronal/synapse

237    biology. Because we observed some paRNAs with exceptional length, we utilized public

238    nanopore long-read direct RNA-seq as an orthogonal method to validate paRNA existence and

239    length (from dorsolateral prefrontal cortex (DLPFC) brain region by the Rush Alzheimer's

240    Disease Study). Defining the lengths of paRNAs is important to assign m6A peaks to these

9

241    paRNA transcripts, because the peaks can sometimes be located >10kb away from the TTSs, as

242    exemplified in **Fig. 2A,B** (and other examples see below). Despite the low coverage and its

243    utilization of polyA capture, long-reads RNA-seq data detected about 25% of paRNAs seen by

244    our *de novo* calling of total RNA-seq data, and the length estimation is highly accurate

245    (**Supplementary Fig. 5C,D**). Globally, paRNA expression levels appeared comparable in

246    Normal and AD mFCs, but those with m6A modifications are expressed higher than those

247    without (**Supplementary Fig. 5E,F**), suggesting a positive influence of m6A methylation on

248    paRNAs expression.

249

250    Differential analysis of paRNAs revealed 88 upregulated and 99 downregulated paRNAs in AD

251    mFC regions (**Fig. 2E,** and **Supplementary Table 6**). These changes are also recapitulated by

252    total RNA-seq data from Normal/AD brains by Nativio et al.[36] (from LTL brain region, **Fig. 2F**).

253    paRNAs altered in AD versus Normal brains are distinct from those changed in normal aging

254    (old versus young human brains that are cognitively normal, **Fig. 2F**), suggesting potential

255    involvement of these RNAs in AD pathogenesis. Interestingly, we found that paRNAs

256    upregulated in AD are much longer than paRNAs downregulated in AD, a pattern not observed

257    for deregulated protein-coding genes (**Supplementary Fig. 5G**). Although it is currently unclear

258    what the molecular basis underlying this observation is, we speculate that there are malfunctions

259    of RNA processing in AD that deregulate paRNAs in a length-related manner. Consistent with

260    the correlation seen for mRNAs and other ncRNAs, hyper- and hypo-methylation of paRNA is

261    correlated with their expression increase and decrease in AD, respectively (**Fig. 2G,H**).
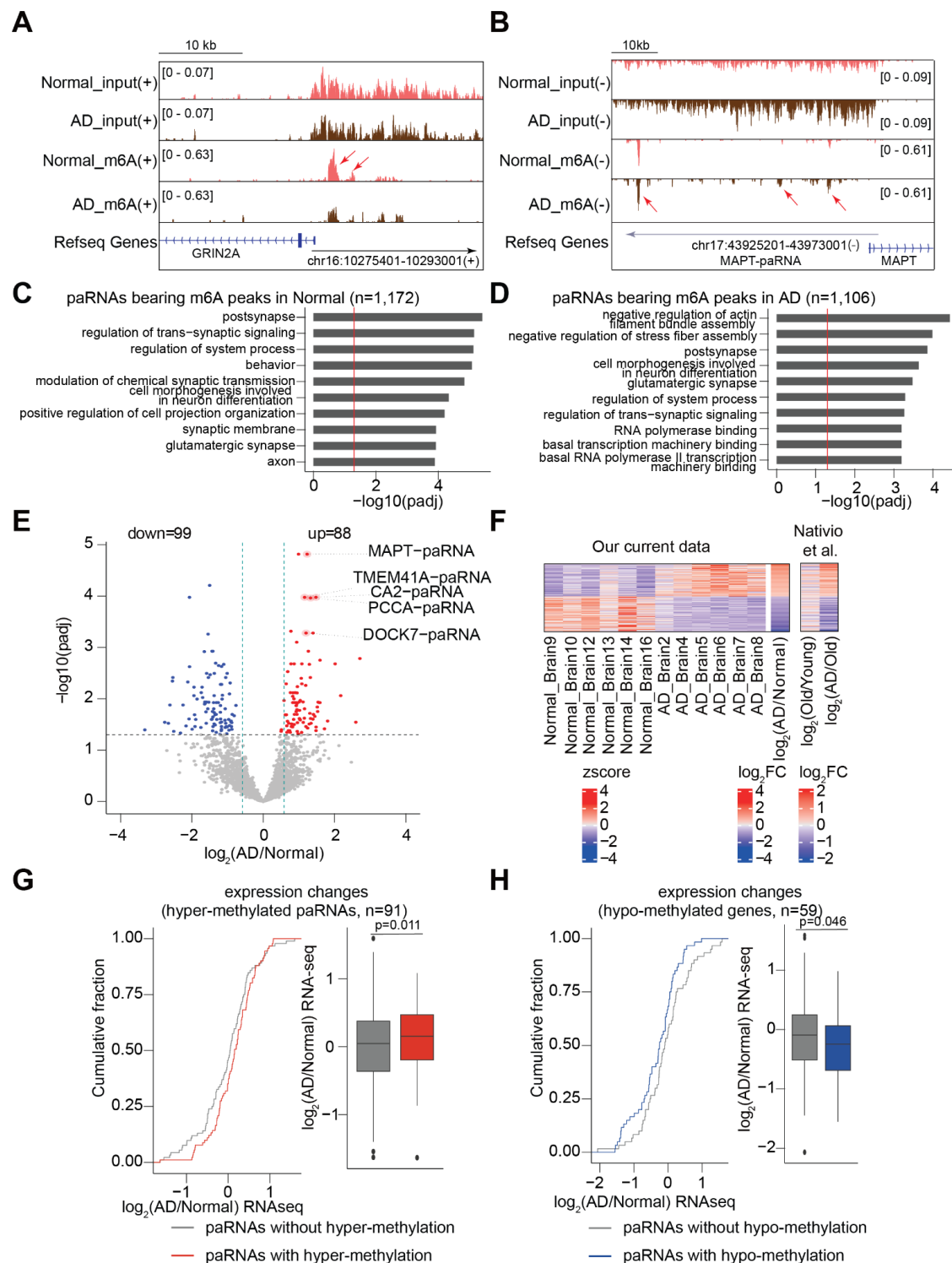
**Figure 2. The m6A methylation and expression of paRNAs in Normal and AD human brains. A,B**. Genome browser tracks showing the RNA-seq and m6A signals of two paRNAs (*GRIN2A-paRNA* and *MAPT-paRNA*) in the human mFC. Red arrows indicate m6A peaks. **C,D**. GO analyses for genes neighboring and sharing promoters with paRNAs. The red lines represent adjusted p values (p-adj) at 0.05. **E**. A volcano plot showing differentially expressed paRNAs between Normal and AD brains. Red and blue dots represent up-regulated and down-regulated paRNAs in AD, respectively. **F**. A heatmap showing z-score-transformed expression levels of differentially expressed paRNAs between Normal and AD brains from our samples, and from Nativio et al.[36]. **G,H.** Cumulative

11

270    distribution and boxplots of paRNA expression changes with or without hyper- and hypo-m6A. P values were
271    calculated by a two-tailed non-parametric Wilcoxon–Mann–Whitney test. Boxplots indicate the interquartile range
272    with the central line representing the median, and the vertical lines extending to the extreme values in the group.
273

274    **paRNA deregulation in AD mouse model and other human neurodegenerative diseases**

275    We examined if the paRNAs deregulated in human AD brains can be detected in 5xFAD mice

276    brain, a well-characterized mouse model of AD[45]. Total RNA-seq data has been generated from

277    the right cerebral hemisphere of 5xFAD mice brain (ID: syn21983020). There are 1,378 paRNAs

278    produced from promoters of homologous genes in human and mice brains (hereafter referred to

279    as common paRNAs) (**Fig. 3A**). Of these, about 6% (n=87) showed altered expression in human

280    AD brains (**Fig. 3B**), and about 3% (n=42) were differentially expressed in the 5xFAD mouse

281    brains versus wild-type controls. However, none of them is consistent between human and

282    mouse AD brains (**Fig. 3B**). Because 5xFAD is mainly an amyloid model, whereas our human

283    RNA-seq data are from patients bearing both Tau and amyloid pathologies, we examined another

284    mouse model exhibiting both these two pathologies, the 3xTg-AD model[46]. Based on the same

285    process done above for 5xFAD, we identified 3,934 paRNAs in 3xTg-AD mouse brains

286    (hippocampus, data from syn22964719). Differential expression analysis identified 5 upregulated

287    and 1 downregulated paRNAs in 3xTg-AD mice (n=18) compared to wild-type (n=18). There

288    are no common differentially expressed paRNAs between 3xTg-AD mouse model and human

289    AD brains (**Fig. 3C**). A similar conclusion is also drawn by comparing paRNA changes in the

290    human brain versus those changes in the P301S mouse brains[47], a commonly used tauopathy

291    model (**Fig. 3D**). Such a lack of similarity of paRNAs altered in human and mouse AD brains is

292    consistent with the idea that AD mouse models cannot completely recapitulate human AD
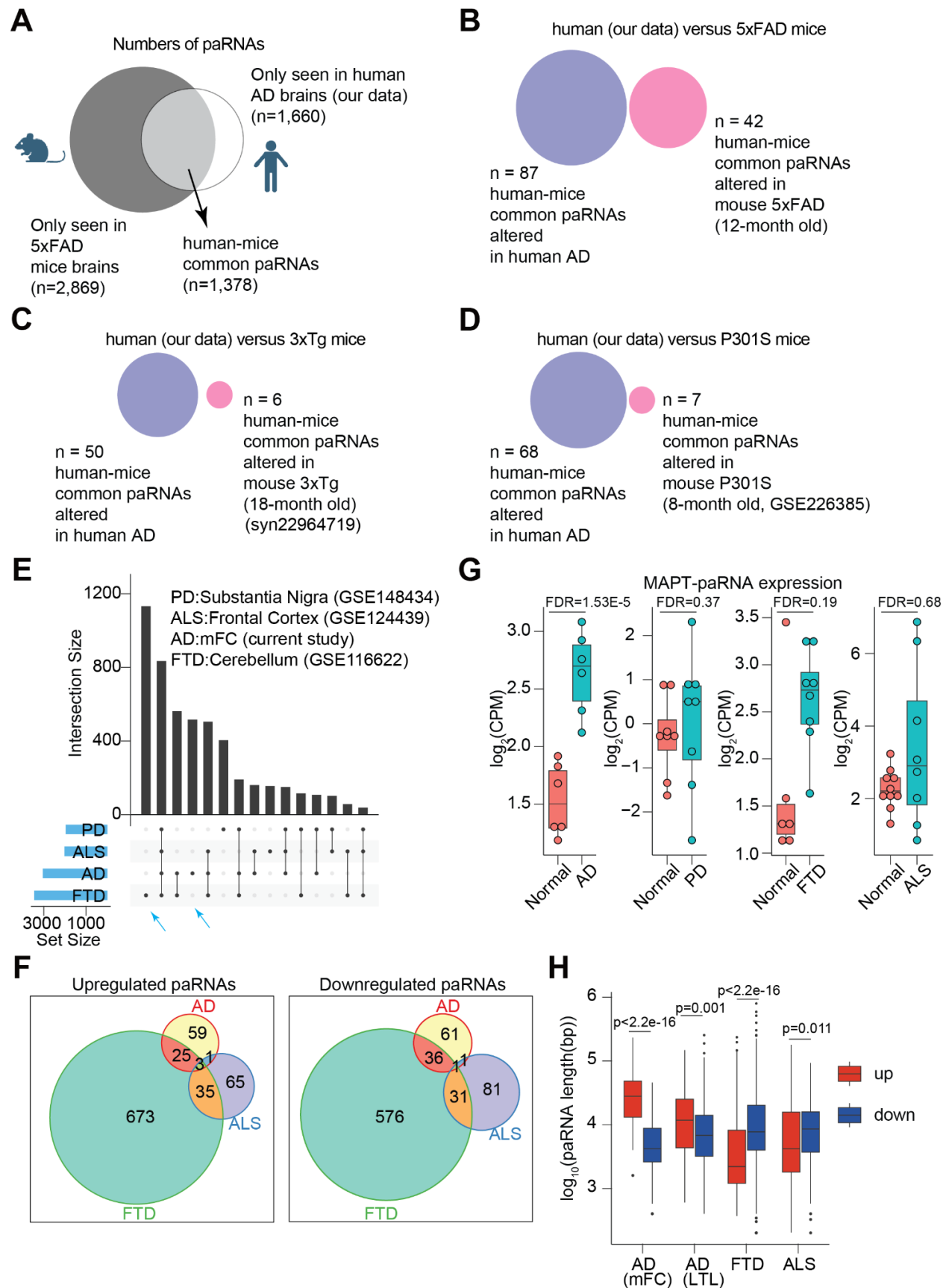
293    pathogenesis[48].

294

295 **Figure 3. Comparing paRNA changes in human AD versus mouse AD models or other human**
296 **neurodegenerative diseases.  A**. A venn diagram showing the numbers of human-mice common and species-
297 specific paRNAs in human and mouse brains, respectively. The human data is from our current work. The mouse
298 data is calculated from RNA-seq datasets generated in brains of a 5xFAD mouse model. Common paRNAs were
299 defined by their production from promoters of homologous genes. **B-D**. Venn diagrams showing dysregulated
300 paRNAs from human-mouse common paRNAs in either human brains or mouse models as indicated. **E**. An UpSet
301 plot showing common and unique paRNAs detected in human brain RNA-seq data generated in donors bearing
302 several neurodegenerative diseases. The datasets information and brain regions are indicated. Blue arrows point to
303 paRNAs uniquely seen in FTD and AD. **F**. Venn diagrams showing the limited overlaps of upregulated and
304 downregulated paRNAs across different neurodegenerative diseases, respectively. **G**. Boxplots showing the
305 expression levels of *MAPT-paRNA* across different neurodegenerative diseases. FDR values were calculated by
306 DESeq2. **H**. Boxplots showing the length of upregulated and downregulated paRNAs across different
307 neurodegenerative diseases. Red and blue boxplots represent upregulated and downregulated paRNAs in each
308 disease, respectively. P values were calculated by a two-tailed non-parametric Wilcoxon–Mann–Whitney test. In all
309 panels, boxplots indicate the interquartile range with the central line representing the median, and the vertical lines
310 extending to the extreme values in the group.

312 We next examined whether any paRNAs are also dysregulated in human brains with other
313 neurodegenerative diseases, such as Parkinson's disease (PD)[49], Frontotemporal Dementia (FTD)
314 [50], and Amyotrophic lateral sclerosis (ALS)[51]. For these, we retrieved RNA-seq datasets for each
315 disease, and identified 1,826 paRNAs in PD, 3,454 in FTD, and 2,007 paRNAs in ALS,
316 respectively, by *de novo* transcript calling (**Fig. 3E**). These paRNAs showed non-overlapping
317 expression patterns in different diseases: for example, more than 500 and 1,000 paRNAs are only
318 found in AD and FTD brain samples, respectively (blue arrows, **Fig. 3E**). We identified
319 deregulated paRNAs in each disease, and these showed limited overlaps (**Fig. 3F**). These results
320 demonstrate disease-specific expression or deregulation of paRNAs, although the contribution of
321 RNA sample quality and different brain regions used in the data generation cannot be fully
322 excluded. For example, *MAPT-paRNA* is expressed in several diseases, but it is upregulated only
323 in the human AD brains (**Fig. 3G**, also see **Fig. 2E**). We observed that the length of upregulated
324 paRNAs was longer than that of downregulated paRNAs in AD brains, which is reproducible by
325 analyzing data from Nativio et al.[36] (**Fig. 3H**). Interestingly, this pattern was not seen or even
326 reversed in ALS and FTD (**Fig. 3H**). These results indicate that paRNAs can be deregulated in
327 several neurodegenerative diseases, but the exact paRNAs and the mechanisms underlying their
328 deregulation can be disease- or context-dependent.

330 **Deregulation of paRNAs in AD does not correlate with promoter epigenetic state changes**
331 As paRNAs and their nearby genes share promoters, their expression levels are expected to be
332 correlated if they are regulated at the transcriptional level by the promoters' epigenetic states
333 (**Supplementary Fig. 6A**). However, when we analyzed AD-associated expression changes of

14

334    paRNAs versus the bidirectional mRNAs from the same promoters, we observed a poor

335    correlation between upregulated paRNAs versus their bidirectional mRNAs (median correlation

336    coefficient R=-0.01, n = 88 pairs); whereas the correlation between AD-downregulated paRNAs

337    and their bidirectional mRNAs is better but remains modest (median correlation coefficient

338    R=0.42, n = 99) (**Supplementary Fig. 6B**). Two representative examples are given, showing an

339    AD-upregulated paRNA from the *CTCF* gene promoter, and an AD-downregulated paRNA

340    antisense to the *VMA21* gene promoter (**Supplementary Fig. 6C**). This phenomenon was

341    recapitulated in another independent AD dataset from the LTL region[36] (**Supplementary Fig.**

342    **6D**). Taking *MAPT-paRNA* as an example, while it is consistently upregulated in AD, its

343    neighboring gene *MAPT* was not significantly changed from either of two brain regions/cohorts

344    we analyzed (**Supplementary Fig. 6E,F**). These findings suggest that AD-deregulated paRNAs,

345    especially those upregulated in AD, are likely altered in a manner decoupled from the nearest

346    mRNA genes; and if these paRNAs may have functions, it is unlikely they impact their

347    promoter-sharing nearby genes.

348

349    We further examined the epigenetic states of deregulated paRNAs. Because we found consistent

350    changes of paRNAs in the LTL regions of AD brains from the study by Nativio et al.[36] (**Fig. 2F**),

351    which generated ChIP-seq data for acetylation of histone H3 at residue K27 (H3K27ac), a

352    histone marker for active promoters/enhancers, we thus tested this question in LTL. We found

353    that the H3K27ac signal around TSSs of deregulated paRNAs was not different between Normal

354    and AD brains (**Supplementary Fig. 6G**). This observation was recapitulated by analyzing

355    ChIP-Seq datasets of H3K27ac and tri-methylation of histone H3 lysine 4 (H3K4me3) generated

356    by a separate AD brain cohort (DLPFC regions, Rush Alzheimer's Study) (**Supplementary Fig.**

357    **6H**). Taking *MAPT* and *TMEM41A* loci as examples, the H3K27ac and H3K4me3 signals on

358    their promoters were similar between Normal and AD brains, despite these two paRNAs being

359    upregulated (**Supplementary Fig. 6I**). In summary, our results indicate that the epigenetic state,

360    at least by the histone markers we examined here at the TSSs, is not associated with paRNA

361    deregulation in AD.

362

363    **Cell-type specific paRNA expression and deregulation in AD**

364    Brain tissue consists of several neuronal and glial cell types. We reanalyzed a publicly available

365    single-nucleus RNA-seq (snRNA-seq) dataset generated from Normal/AD human brains[52]

366    (DLPFC region) to appreciate expression patterns of paRNAs in different cell types. Different

367    numbers of Unique Molecular Identifiers (UMIs) and cells of each major type were observed

368    (**Supplementary Fig. 7A,B**). In total, 763 and 872 paRNAs we identified by bulk RNA-seq data

369    of mFC can be detected by DLPFC snRNA-seq in Normal or AD conditions, respectively

370    (**Supplementary Fig. 7C**), among which, m6A-marked paRNAs were more detectable

371    (**Supplementary Fig. 7D,E**). These numbers were broken down to cell-type-specific patterns,

372    and excitatory neurons (Ex) possess the largest numbers of paRNAs detected (**Supplementary**

373    **Fig. 7F**). Among paRNAs seen in snRNA-seq data, about 30% (n=284) are exclusively detected

374    in neurons (excitatory, Ex; or inhibitory, In), and a smaller group of paRNAs (n=69) are

375    exclusively detected in glial cell types (such as astrocytes, Ast; oligodendrocytes, Oli; or

376    microglia, Mic; **Supplementary Fig. 7F**). For the top five highly AD-upregulated paRNAs (**Fig.**

377    **2E**), they all displayed a certain degree of cell-type-specificity (**Supplementary Fig. 7G**). For

378    example, *DOCK7-paRNA* was highly expressed in Ast; *MAPT-paRNA* is expressed higher in Ex

379    and In, and to some degree in Oli (**Supplementary Fig. 7G**). By comparing Normal and AD

380    conditions in each cell type, *MAPT-paRNA* was significantly increased in AD only in Ex

381    (**Supplementary Fig. 7H**). This paRNA is annotated as *MAPT-AS1* in the Gencode database, but

382    for consistency in this paper, we will refer to it as *MAPT-paRNA*. These results indicate that

383    paRNAs are expressed in the human brain and altered in AD with cell-type-specificity.

384

385    **m6A methylation regulates stability of paRNAs**

386    We searched for appropriate cell models to study the potential roles of AD-associated paRNAs

387    and the impact of m6A. In major iPSC-derived brain cells where RNA-seq data are available[53],

388    each of the top five AD-deregulated paRNAs was found to display some level of cell-type-

389    specificity, but they are more often expressed highly in neurons (**Supplementary Fig. 8A**).

390    Among these, *MAPT-paRNA* exhibited the highest and almost exclusive expression in iPSC-

391    derived neurons (**Supplementary Fig. 8A**). It is notable that the cell-type-specificity of paRNAs

392    revealed by DPFLC snRNA-seq data differs from that by bulk RNA-seq from iPSC derived cells

393    (**Supplementary Figs. 7G, 8A**), indicating that cell models can only partially recapitulate

394    paRNA expression patterns in adult and/or AD human brains.

16

395     *MAPT* is a central disease locus in AD, because it encodes for the Tau protein that drives

396     neurofibrillary tangles in AD brains[3]. A previous study reported that *MAPT* nature antisense

397     transcript (NAT), which largely overlaps and is essentially *MAPT-paRNA*, represses *MAPT*

398     translation to Tau protein in SH-SY5Y cell line[33]. However, another study found that *MAPT-*

399     *paRNA* does not impact *MAPT*/Tau at either the transcriptional or translational levels[34].

400     Consequently, the functional role of *MAPT-paRNA* in AD remains unclear. We thus elected to

401     focus on *MAPT-paRNA* for in depth experimental studies. We first tested the expression of

402     *MAPT-paRNA* in cellular models, including human embryonic stem cells (H1-ESCs), a human

403     microglia cell line (HMC3), a human neuroblastoma cell line (SH-SY5Y), H1-hESC-derived

404     astrocytes, neural progenitor cells (NPC), and iPSC-derived microglia and neurons (i3Neurons)

405     (see methods, **Fig. 4A**). Quantitative reverse-transcription PCR (qRT-PCR) results confirmed

406     that *MAPT-paRNA* is highly and almost exclusively expressed in i3Neurons as compared to other

407     cell types (**Fig. 4A**). The i3Neurons we generated are based on a doxycycline (Dox) inducible

408     NGN2-directed differentiation method of WTC11 iPSCs[54], which are glutamatergic excitatory

409     neurons that displayed well-recognized neuronal maturation processes by both morphology and

410     molecular markers (**Supplementary Fig. 8B,C**). Three weeks after in vitro differentiation (IVD),

411     these neurons started to express *MAP2*, a neuronal marker, and by 6-8 weeks, they showed

412     prominent expression of synaptic markers, such as postsynaptic density protein 95 (PSD95)

413     (**Supplementary Fig. 8B,C**). *MAPT-paRNA* appeared to gradually increase expression during

414     neuronal maturation and its level plateaued at around 5 weeks IVD (**Supplementary Fig. 8D**).

415     To investigate how m6A methylation may impact *MAPT-paRNA* expression, we treated 8-week-

416     old i3Neurons with STM2457[55], a chemical inhibitor of m6A writer METTL3. Antibody based

417     m6A RIP-qPCR showed that this treatment reduced the m6A methylation level of *MAPT-*

418     *paRNA*, which resulted in its expression decrease as shown by RT-qPCR (**Fig. 4B,C**). These

419     results suggest that m6A positively regulates *MAPT-paRNA* expression. In contrast, this

420     treatment did not impact either the mRNA expression or transcription level of *MAPT*, which

421     shares the same promoter with the paRNA. These are revealed by using primers targeting the

422     mRNA (across exons) or the intronic regions (indicating pre-mRNA transcription), respectively

423     (**Supplementary Fig. 8E**). These results indicate that m6A inhibition did not reduce *MAPT-*

424     *paRNA* level via altering the transcriptional activity of the shared promoter, which otherwise

425     would have affected *MAPT* transcription as well. We further examined if the observed *MAPT-*

426      *paRNA* reduction takes place at the RNA stability level, and found that after transcriptional

427      inhibition, the paRNA with a lower m6A level (i.e., presence of STM2457) displayed a lower

428      stability and faster decay (**Fig. 4D**). We additionally conducted genetic knockdown (KD) of

429      METTL3 by an antisense oligonucleotide (ASO) in 8-week old i3Neurons (**Supplementary Fig.**

430      **8F,G**), which reduced both m6A modification and RNA expression level of *MAPT-paRNA*

431      (**Supplementary Fig. 8H,I**), consistent with the results from the chemical inhibitor treatment.

432

433      ***MAPT-paRNA* regulates global gene transcription in human neurons *in cis* and *in trans***

434      We further studied the functions of *MAPT-paRNA* by employing ASOs to KD it in 8-week IVD

435      excitatory i3Neurons, because at this stage, neurons possess maximal level of expression of this

436      paRNA, displaying prominent neuronal morphology and synaptic features (**Supplementary Fig.**

437      **8B,C**). Gymnotic delivery of ASO achieved potent KD of *MAPT-paRNA* (>80% reduction)

438      without affecting neuronal viability or morphology (**Fig. 4E, and Supplementary Fig. 9A**). We

439      found that KD of *MAPT-paRNA* did not alter *MAPT*/Tau at either the transcriptional or

440      translational levels in i3Neurons (no matter if it is the mRNA, the Tau protein, or the

441      phosphorylated Tau (p-Tau) that is implicated in AD pathology), even after an extended 7-day

442      KD (**Supplementary Fig. 9B,C**). This indicates that *MAPT-paRNA* did not regulate the

443      neighboring gene, *MAPT*, consistent with the report by Policarpo, et al.[34]. No change of

444      *MAPT*/Tau was seen after the KD of *MAPT-paRNA* in SH-SY5Y cells, either (a neuroblastoma

445      cell model used by a prior study of MAPT-paRNA[33]) (**Supplementary Fig. 9D,E**). This result is

446      consistent with the fact that paRNAs upregulated in AD show poor correlation with changes of

447      their bidirectional mRNAs (**Supplementary Fig. 6A,B,D,E,F**).
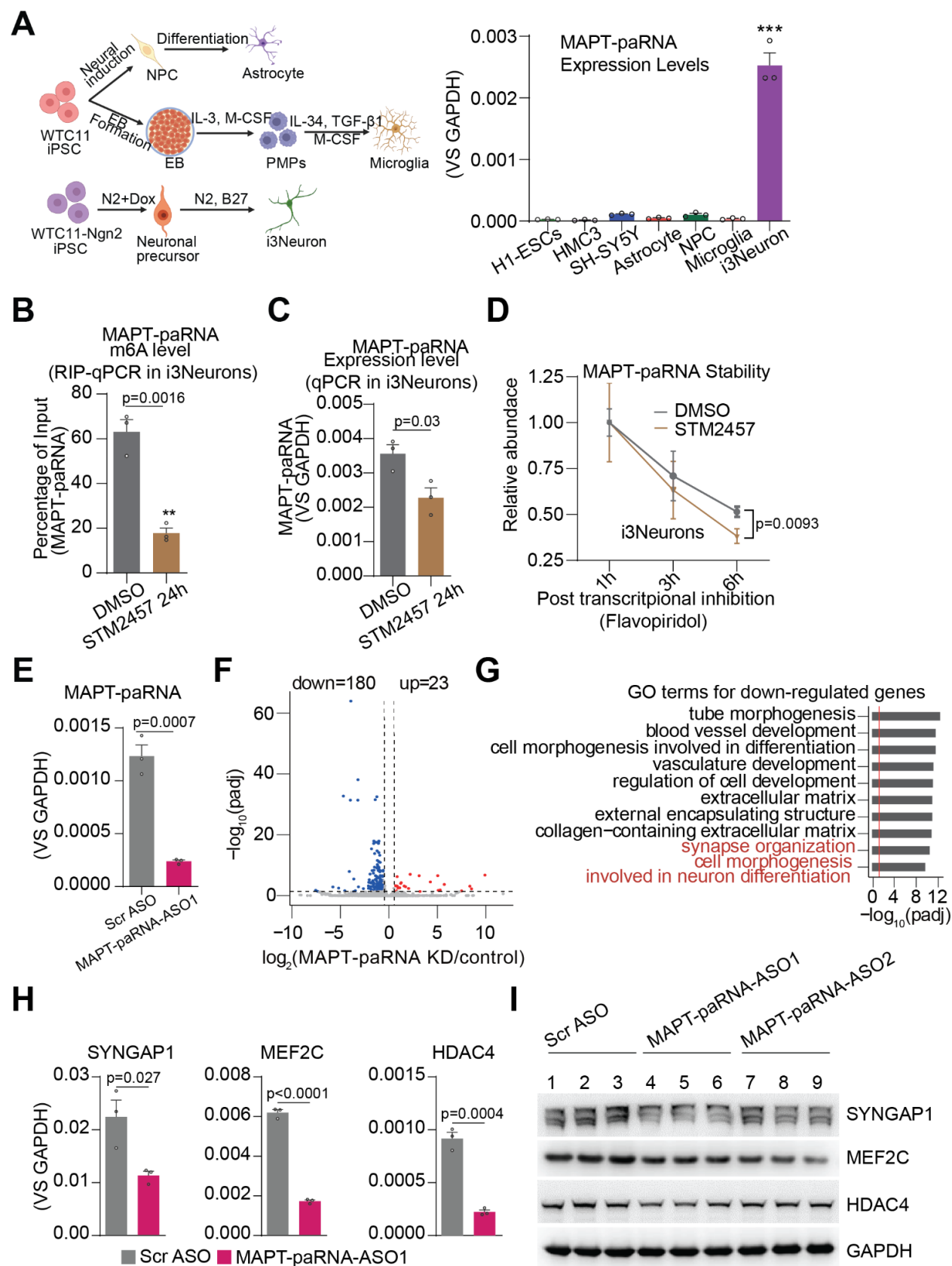
448

449　**Figure 4. Neuron-enriched *MAPT-paRNA* stability control by m6A and its global regulatory functions. A.**
450　(Left) Cartoon diagrams illustrating the differentiation of iPSC-derived brain cells (created with BioRender.com).
451　(Right) A barplot showing the expression levels of *MAPT-paRNA* in various cell types. P value was calculated by a
452　two-tailed student's t-test. **B,C**. MeRIP-qPCR and RT-qPCR data showing m6A methylation and *MAPT-paRNA*
453　expression with and without STM2457 treatment, respectively. **D**. Time course stability of *MAPT-paRNA* measured
454　by RT-qPCR after transcriptional inhibition, with and without STM2457 pre-treatment for 24hr. P value was
455　calculated by a two-tailed student's t-test. **E**. A barplot showing the relative RNA expression of *MAPT-paRNA*
456　quantified by RT–qPCR after scramble or targeting ASO treatment. **F**. A volcano plot showing differentially
457　expressed genes after *MAPT-paRNA* knockdown using a targeting ASO versus the scramble ASO treatment. Red
458　and blue dots represent upregulated and downregulated genes, respectively. **G**. GO analysis for the downregulated
459　genes after *MAPT-paRNA* knockdown. The red line represents adjusted p values (padj) at 0.05. **H**. Barplots showing
460　relative RNA expression of *MEF2C*, *SYNGAP1*, and *HDAC4* quantified by RT–qPCR. P values were calculated by a
461　two-tailed student's t-test. **I**. Protein levels of *MEF2C*, *SYNGAP1*, and *HDAC4* showing triplicates of Western
462　blotting (WB) after *MAPT-paRNA* knockdown.

463

464　To unbiasedly explore its functions, we performed RNA-seq after *MAPT-paRNA* KD. This

465　revealed over 200 genes deregulated, with most of them showing downregulation (n=180), and a

466　smaller subset upregulation (n=23) (**Fig. 4F,** and **Supplementary Table 8**). RNA-seq also

467　confirmed qPCR data that *MAPT* mRNA was not changed (**Supplementary Figs.9B,10A**). GO

468　analysis revealed that the functions of these downregulated genes are closely related to synaptic

469　functions (**Fig. 4G**, and **Supplementary Table 9**). Among these, some are known to be

470　important regulators of neuronal/synaptic biology, such as *SYNGAP1*[56], *MEF2C*[57], and *HDAC4*[58]

471　(**Supplementary Fig. 10B,C,D**). We validated the expression reduction of these "target genes"

472　of *MAPT-paRNA* by RT-qPCR (**Fig. 4H**) and by a second ASO (**Supplementary Fig. 10E**).

473　Consistently, the protein levels encoded by these target genes were also decreased (**Fig. 4I**, and

474　**Supplementary Fig. 10F**). These results demonstrated that *MAPT-paRNA* is a global regulator

475　of gene expression that selectively impacts neuronal/synaptic functions. Interestingly, very few

476　of these target genes are located in its genomic vicinity, and most of them are on different

477　chromosomes (**Supplementary Fig. 10G**), suggesting that *MAPT-paRNA* regulates target gene

478　expression both *in cis* and *in trans*. This is a distinct function from the reported action of some

479　paRNAs that impacts the bidirectional gene sharing promoter with them[27,28].

480

481　**Functional paRNA-target-gene interactions in 3D nucleus revealed by single-cell RNA-**

482　**DNA interactome**

483　A plausible mechanism underlying paRNAs' roles in gene expression control is that they may

484　directly interact with target genes via spatial proximity in a 3D nucleus. To explore this, we

485　analyzed recent single nuclei RNA-DNA interactome data of the human brain (DLPFC region),

20

486   namely by the Multi-Nucleic Acid Interaction Mapping in Single Cell (MUSIC) technique[59]

487   (**Fig. 5A**). MUSIC employs cell barcodes (CB) to define molecules (DNA or RNA) from the

488   same cell, and then uses molecular barcodes (MB) to identify shared molecular complexes that

489   define interactions of DNAs or RNAs (**Fig. 5A**, **see methods**). It provides single cell RNA-DNA

490   interactome and thus can reveal paRNAs' cell-type specific target genes. The cell numbers and

491   gene expression counts from our analysis of the MUSIC datasets are shown in **Supplementary**

492   **Fig. 11A,B** and are identical to what was originally reported[59].

493

494   Overall, 425 paRNAs can be detected in MUSIC data in at least one of the cell types. Among

495   these, Ex exhibited the largest number of detectable paRNAs (n = 393, **Fig. 5B**). This is perhaps

496   partially because our paRNA list was identified in bulk brain RNA-seq data in which neuronal

497   signals are dominant [38], and partially it may also be due to higher detectable RNA reads in Ex in

498   MUSIC data (**Supplementary Fig. 11A,B**). For each paRNA, MUSIC identified their interacting

499   genes in the 3D nucleome based on shared CBs and MBs (**Fig. 5A, see methods**). Ex and Ast

500   exhibited 106 and 17 paRNAs that are specific/exclusive to these two cell types, respectively

501   (**Fig. 5B**). We identified genes showing RNA-DNA contacts with these cell-type-specific

502   paRNAs in their respective cell types, and found 4,736 interacting genes for Ex-specific paRNAs

503   and 1,055 genes for Ast-specific paRNAs. GO analysis of these paRNA-interacting genes

504   revealed them to be related to neuron differentiation/synapse in Ex and cell-cell adhesion in Ast

505   (**Supplementary Fig. 11C**), respectively, suggesting that cell-type-specific paRNAs may play

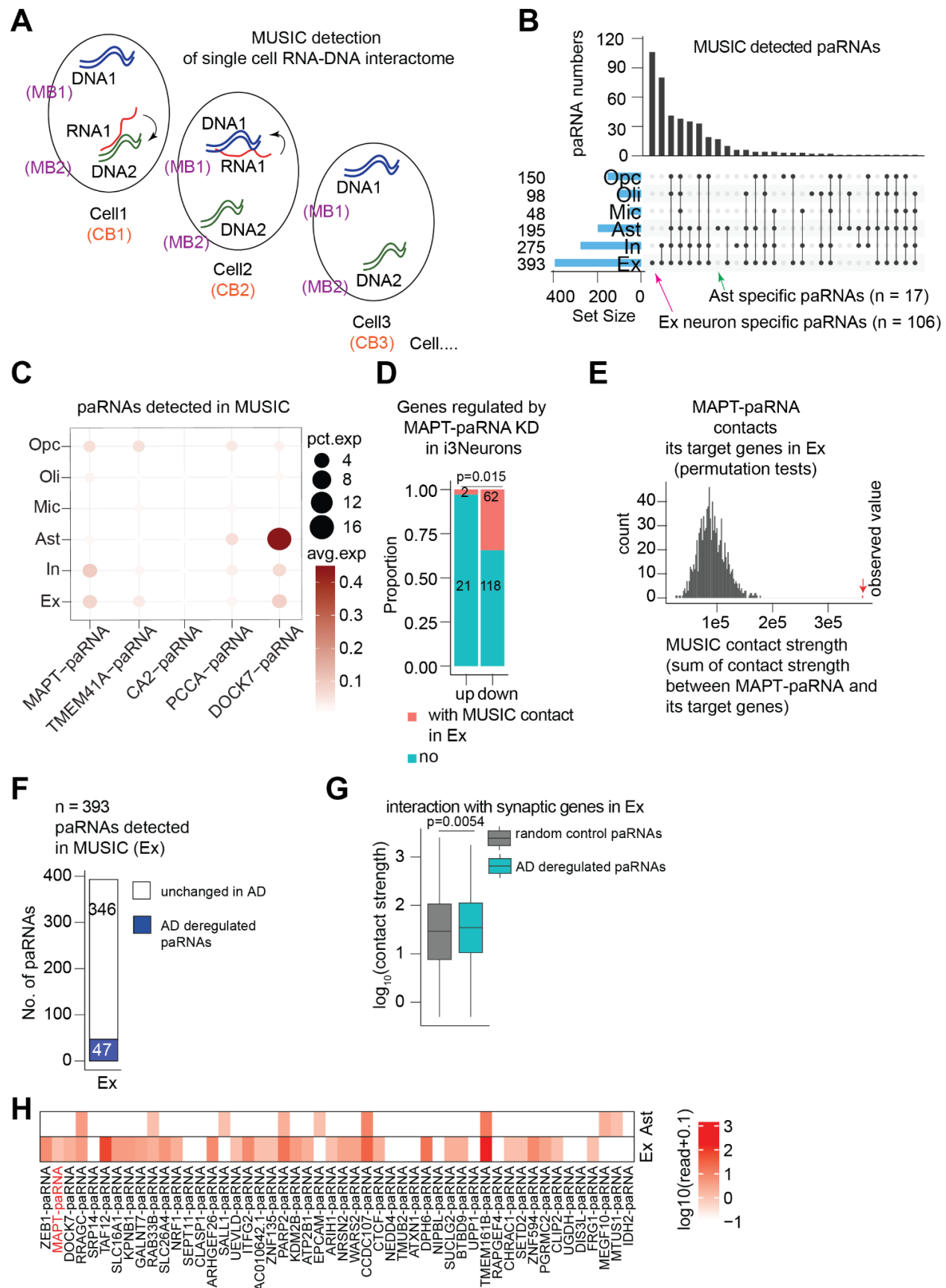506   roles in regulating cell-type-specific genes and cellular functions.

**Figure 5. paRNA-DNA interaction in human brain cells revealed by MUSIC data. A**. A diagram showing RNA-DNA interaction at single-cell level in MUSIC data using cell barcodes (CB) and molecular barcodes (MB). CB is shared by all molecules in one cell, and MB is shared by all molecules in one molecular complex. **B**. An UpSet plot showing paRNAs and their numbers (to the left) in different cell types detected by MUSIC from Normal brain. **C**. A dotplot showing the average expression of the top five AD-upregulated paRNAs in MUSIC data. Ex: Excitatory neurons. In: Inhibitory neurons. Ast: Astrocyte. Mic: Microglia. Oli: Oligodendrocyte. Opc: Oligodendrocyte progenitor cell. **D**. A barplot showing the numbers of differentially expressed genes seen after MAPT-paRNA KD that form RNA-DNA interactions with *MAPT-paRNA* in the Ex neurons. P value: Fisher's exact test. **E**. A barplot from permutation test showing the observed contact strength between MAPT-paRNA and its true 62 target genes (red arrow to the right) versus contact strength between MAPT-paRNA and 1000 sets of randomly selected 62 genes. **F**. A barplot showing the number of paRNAs detected by MUSIC data in Ex neurons and the subset that show AD-deregulation in bulk RNA-seq data in Fig.2. **G**. A boxplot showing the RNA-DNA contact strength between the two groups of paRNAs and synaptic genes in Ex: AD-deregulated paRNAs (n = 47 in panel F), and non-AD-deregulated paRNAs (n = 346). P value: two-tailed non-parametric Wilcoxon–Mann–Whitney test. Boxplots indicate the interquartile range with the central line representing the median, and the vertical lines extending to the extreme values in the group. **H**. A heatmap showing the RNA-DNA contact strength between AD-deregulated paRNAs and a single *MEF2C* gene detected in Ex and Ast, respectively.

We found that m6A-paRNAs can be better detected by the MUSIC data than non-m6A-modified paRNAs, and this is consistent in all cell types (**Supplementary Fig. 11D,E**). This pattern is similar to that in snRNA-seq data (**Supplementary Fig. 7D,E**). As compared to non-m6A-paRNAs, m6A-paRNAs on average can interact with more genes, and show higher interaction strength with genes they contact, a trend particularly obvious in Ex (**Supplementary Fig. 11F**). These results support a notion that m6A-paRNAs are more detectable in MUSIC data possibly due to higher stability, and they possess higher propensity to act in target gene regulation, particularly in Ex. The top five AD-upregulated paRNAs display expression in two or three cell types in MUSIC data (**Fig. 5C**), again a pattern similar to that revealed by snRNA-seq (**Supplementary Fig. 7G**). As aforementioned, KD of *MAPT-paRNA* in i3Neurons, a model of human excitatory neurons, deregulated ~200 genes (**Fig. 4F,G**), many of which are important for neuron differentiation and synapse organization. To test the mechanisms, we examined if *MAPT-paRNA* forms direct RNA-DNA contacts with these "target genes", and we found that about 30% of them (up=2 and down=62) indeed displayed MUSIC RNA-DNA contacts in Ex (**Fig. 5D**). Given that only 2 upregulated genes interact with *MAPT-paRNA*, we will focus on the 62 downregulated "target genes" interacting with *MAPT-paRNA*. The observed contact strength between *MAPT-paRNA* and these 62 target genes was much higher than by random chance (**Fig. 5E**), as shown by permutation tests, for which we randomly selected 62 genes 1,000 times, and calculated the contact strength between *MAPT-paRNA* and each of these random genesets. The contacts between *MAPT-paRNA* and the 62 target genes were more pronounced in Ex than in In

546     or Ast (**Supplementary Fig. 11G**), lending support to the notion that *MAPT-paRNA* contacts

547     these genes and functionally activates their expression specifically in Ex.

548

549     We attempted to test whether this notion may apply to other paRNAs in Ex; i.e., do many of

550     them contact synapse/neuronal genes to potentially play roles in gene regulation and in AD? Out

551     of 393 detectable paRNAs in Ex in MUSIC data, 47 were deregulated in our bulk RNA-seq data

552     (**Fig. 5F**). We calculated RNA-DNA contact strength of each of these paRNAs with a curated set

553     of synapse-associated genes (n = 393, see methods about this curated list), and we found that

554     paRNAs deregulated in AD, as compared to average paRNAs, display higher interaction

555     frequency with synapse-associated genes in Ex (**Fig. 5G**). As an example, RNA-DNA contacts

556     were found in Ex to form between not only *MAPT-paRNA,* but also a series of other AD-

557     deregulated paRNAs, with *MEF2C* (encoding a key neuronal factor known to confer resilience to

558     AD[47,60])(**Fig. 5H**). In contrast, these interactions did not take place in Ast (**Fig. 5H**). These

559     results support that at least a subset of neuronal paRNAs, as exemplified by *MAPT-paRNA*, can

560     contact and regulate neuronal/synapse genes; alteration of such paRNAs in AD are involved in

561     deregulation of key synaptic genes and AD pathogenesis.

562

563     **_MAPT-paRNA_ protects neurons from excitotoxicity by modulating synaptic activity**

564     An important feature of AD is neuronal hyperexcitability, which leads to excitotoxicity and

565     neuronal death[61,62]. This is often mediated by an overactive N-methyl-d-aspartate receptor

566     (NMDAR) at the synapse. Several key synaptic genes dependent on *MAPT-paRNA*, such as

567     *MEF2C* and *SYNGAP1* (**Fig. 4G,H**), have been known to modulate NMDA activity at synapses

568     [63-65]. Indeed, *Mef2c* deletion in mice impairs learning and memory[66], and it has been shown to

569     prevent neuronal apoptosis elicited by excitotoxic NMDA[65]. Loss of *SYNGAP1* induces neuronal

570     hyperexcitability, leading to deficits in learning and memory[67]. These results suggest that *MAPT-*

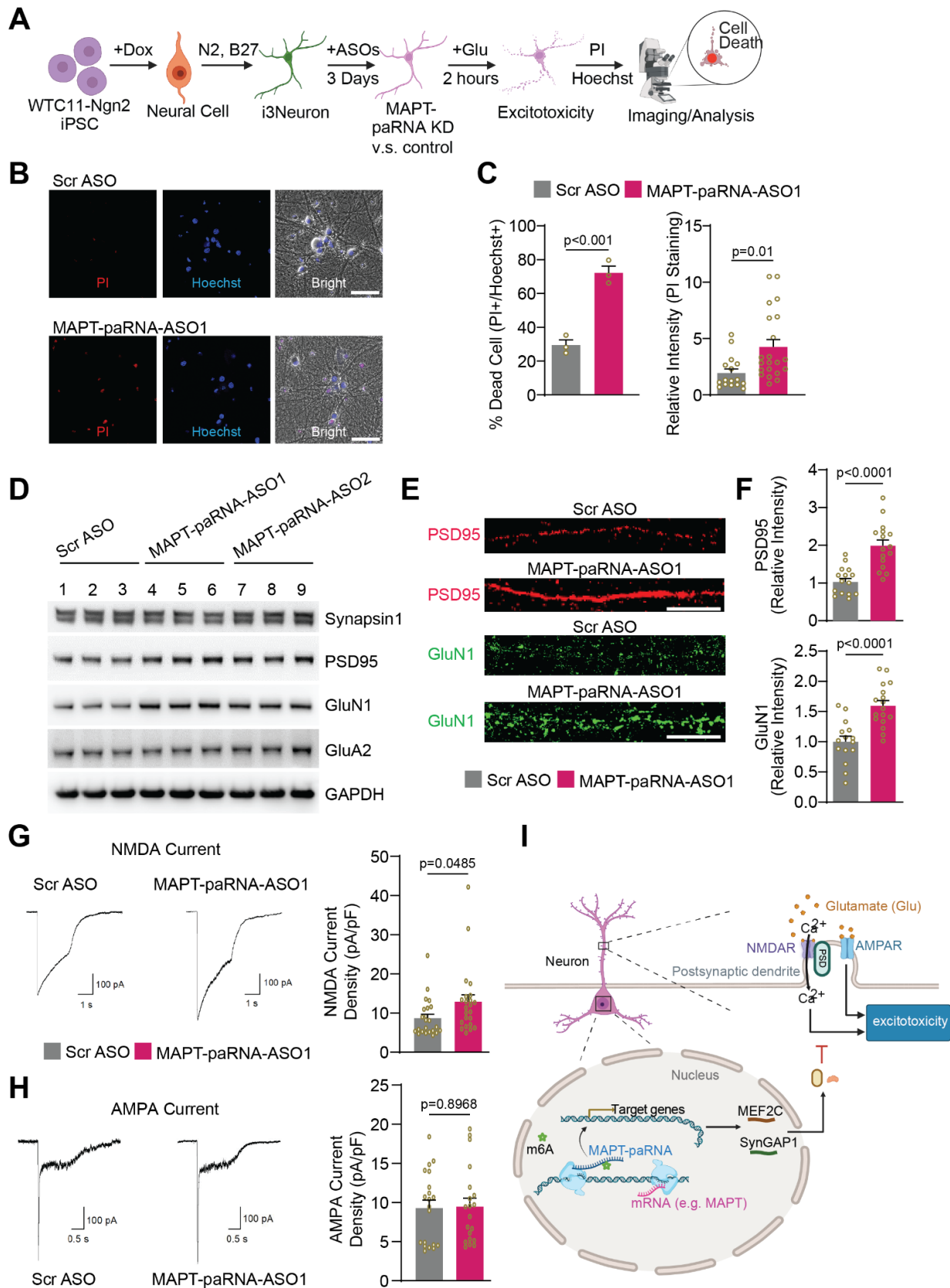571     *paRNA* might act as a neuroprotective modulator in the context of AD.

572

25

**Figure 6. The neuroprotective role of *MATP-paRNA* against excitotoxicity. A**. Schematic representation of glutamate toxicity in WTC11-derived i3Neurons. 8-week-old i3Neurons with/without *MAPT-paRNA* knockdown were treated with 10μM glutamate for 2 hours. PI (propidium iodide) and Hoechst 33342 were introduced to the medium to visualize dead (PI+) and total (Hochest+) cells, respectively. **B**. Representative images showing glutamate-induced i3Neuron cell death after *MAPT-paRNA* knockdown. Scale bar, 50μm. **C**. Quantification of apoptotic i3Neurons from panel B. **D**. Triplicates of western blot analysis of synaptic markers (Synapsin1 and PSD95) and glutamate receptors (GLUN1 and GLUA2) in i3Neurons after *MAPT-paRNA* knockdown. **E**. Representative images showing immunofluorescent signals of PSD95 and GluN1 at the dendrites of i3Neurons after *MAPT-paRNA* knockdown, showing their accumulation. Scale bar, 10μm. **F.** Quantitative analysis of signals in panel **E**. For each group, at least 15 neurons from 3 different experiments were quantified and analyzed. **G.** Representative NMDA current traces (left panel) and current density comparison (right panel) from i3Neurons treated with scramble control and *MAPT-paRNA* ASO1 (n = 23 neurons per group). **H**. Representative AMPA current traces (left panel) and current density comparison (right panel) from i3Neurons treated with scramble control and *MAPT-paRNA* ASO1 (n = 20 neurons per group). **I**. A model of *MAPT-paRNA* function, as a representative m6A-modified ncRNA in AD, in neuronal gene regulation and survival (generated by Biorender). P values: two-tailed unpaired student's t-tests were used for **C, F, G**, and **H**.

To test this, we employed an AD-relevant glutamate-induced excitotoxicity model[68,69] (**Fig. 6A**). We found that mature i3Neurons (8-week IVD) with *MAPT-paRNA* KD are more vulnerable to glutamate-induced cell apoptosis, as shown by significantly higher numbers of cells showing Propidium Iodide (PI) staining (**Fig. 6B,C**). Since SYNGAP1 and MEF2C have been reported to inhibit excitotoxicity by modulating the levels of postsynaptic proteins and glutamate receptors, we selected four of these proteins/receptors to test, finding PSD95 and GluN1 (glutamate NMDA Receptor 1) significantly increased in i3Neurons after *MAPT-paRNA* knockdown, while Synapsin1 (a presynaptic protein) and GluA2 (glutamate AMPA Receptor subunit 2) were not changed (**Fig. 6D**, and **Supplementary Fig. 12A**). These changes did not take place at the mRNA levels (**Supplementary Fig. 12B,C**), consistent with the reports that SYNGAP1 or MEF2C modulate post-synapse proteins and excitability locally at the synapse[70,71]. We also conducted KD of *MEF2C* and *SYNGAP1* mRNAs by ASOs, and these caused upregulation of PSD95 and GluN1, but not GluA2, a pattern consistent with *MAPT-paRNA* KD (**Supplementary Fig. 12D,E,F**). Furthermore, immunostaining after *MAPT-paRNA* KD directly showed accumulation of PSD95 and GluN1 at the dendrites of i3Neurons  (**Fig. 6E,F**). Importantly, neuronal electrophysiology confirmed alteration of NMDA receptor activity after KD of this paRNA, while AMPA receptor activity was unaffected (**Fig. 6G,H**). The protective role of *MAPT-paRNA* also applies to beta-amyloid (Aβ-42)-induced neuronal cytotoxicity[72,73], as revealed by increased lactate dehydrogenase (LDH) release in the culture media if i3Neurons were depleted of this paRNA (**Supplementary Fig. 12G**). All together, these results indicate that *MAPT-paRNA* exerts neuroprotective effects, at least in part, via regulating the expression of key

26

611    synapse-associated genes to modulate the distribution and assembly of synaptic scaffolding

612    proteins and glutamate receptors (**Fig. 6I**).

613

614    *Discussion*

615    **m6A methylome on coding and noncoding RNAs in human brain and AD**

616    Our current study utilized total RNA-seq and m6A RIP-seq datasets in human brain samples

617    from AD patients or cognitively normal controls, and identified a comprehensive landscape of

618    RNA m6A methylome on mRNAs and ncRNAs. Our results showed that about 60-70% of m6A

619    peaks in the human mFC are located in the noncoding regions (**Fig.1A,** and **Supplementary Fig.**

620    **2H**), encompassing various categories of ncRNAs. These include annotated lncRNAs or other

621    ncRNAs (e.g., snoRNAs and snRNAs), as well as ncRNAs that have not been previously

622    annotated in the human transcriptome (Gencode database), including many paRNAs that we

623    focused on in the latter part of this work. Interesting, we observed around 8,000 highly m6A-

624    marked intronic regions that overlap with L1 elements. These intronic m6A-marked L1s have

625    been identified by our previous work in cancer cells, fetal human brains, and iPSC-derived

626    neural progenitor cells[12], in which we dubbed them m6A-marked intronic L1s (MILs) and found

627    they can impact the transcription of the genes that harbor them. While in this current work we

628    focus on paRNAs for functional studies because they have been less explored, it will be

629    interesting and important to further test the roles of various m6A-modified ncRNAs in gene

630    regulation, cellular functions in the human brain, and in AD pathogenesis. Therefore, our current

631    work offers an m6A methylome that has significantly extended the previous observations of

632    m6A on mRNAs in normal human brains or in diseased brains from AD or ALS[19,74].

633

634    Our RNA-seq transcriptome data captured known features of the AD brain, including reduced

635    expression of synapse-related genes, and this pattern is consistent with other recent datasets[36].

636    Interestingly, the changes of m6A methylome in normal and AD conditions are not particularly

637    pervasive, i.e., we identified 835 and 1,645 regions showing m6A hypo- and hyper-methylation.

638    This selective and moderate m6A change in AD is consistent with the fact that we did not

639    observe strongly changed gene expression of m6A modifying enzyme genes in AD brains, such

640    as *METTL3* and *METTL14.* In addition, we observed a moderate but significant positive

641    correlation between m6A changes and ncRNA expression changes (**Supplementary Fig. 4A,B**).

642    This indicates that collectively m6A modification may play a positive role in regulating ncRNA

643    expression in human brains. However, it is noteworthy that m6A is by no means the only

644    mechanism that impacts the expression of these ncRNAs in the brain or in AD, and thus it is not

645    surprising that the positive correlation is not particularly strong. Knockdown of METTL3, the

646    main m6A enzyme, quantitatively affected *MAPT-paRNA* expression (**Supplementary Fig.**

647    **8F,G,I**). Other mechanisms affecting ncRNA expression in AD can be from the levels of

648    transcriptional/epigenetic control and other non-m6A-mediated RNA stability regulation.

649

650    **Expression patterns and regulation of paRNAs in neurodegeneration**

651    We identified 3,038 paRNAs in the human brain mFC region via *de novo* transcript calling, and

652    found that close to 40% of them harbor m6A methylation. Interestingly, the genes neighboring

653    m6A-marked paRNAs show enrichment of terms like synapses, indicating that paRNAs are

654    produced and methylated selectively from important synapse/brain associated loci. By

655    comparing paRNA landscapes we detected in human AD brain with those from mouse AD

656    models, or from brain samples with other neurodegenerative diseases (NDDs), our study

657    supports a conclusion that human AD-associated paRNAs are quite unique to human AD, and

658    not commonly seen changed in other NDDs that we analyzed. These results demonstrate that

659    paRNAs are potentially disease specific ncRNAs that play roles in gene dysregulation or disease

660    etiology of NDDs.

661

662    Our analysis of available epigenetic datasets supports that AD-deregulated paRNAs, particularly

663    those that show upregulation in AD, are unlikely to be altered at the epigenetic levels, as

664    H3K4me3 and H3K27ac signals at their transcriptional start sites are similar in Normal and AD

665    conditions. The expression changes of paRNAs and paired promoter-sharing mRNAs displayed

666    poor correlation, too. This argues against that transcriptional/epigenetic deregulation is a main

667    reason for paRNA alteration in AD, as this otherwise should deregulate the promoter-sharing

668    gene mRNAs in a correlated manner. These results suggest a possibility that paRNA

669    deregulation in AD may happen at the post-transcriptional level, likely as a consequence of

670    defective RNA processing. Consistent with this, chemical inhibition of m6A reduces the stability

671    of *MAPT-paRNA* from a key AD locus (i.e., *MAPT*), lending support that m6A methylation acts

672    as at least one of the mechanisms in AD that can impact paRNA expression via stability control.

**673** ***MAPT-paRNA* does not regulate neighboring *MAPT* mRNA or Tau protein levels**

**674** Given the central role of Tau protein in the pathology of AD and other neurodegenerative

**675** diseases, the locus coding Tau, *MAPT*, has been actively investigated to understand its mRNA

**676** expression and translational control[75]. AD-associated genetic variants exist in this locus[76,77], and

**677** ncRNAs are produced therein. It is important to discover AD-associated ncRNAs that can

**678** regulate *MAPT*/Tau expression, which may offer mechanistic insights into Tauopathy in AD and

**679** potentially new therapeutic avenues. Simone et al. reported that natural antisense transcripts

**680** (named NAT in their work), which is essentially *MAPT-paRNA*, can play a role to suppress

**681** *MAPT* mRNA translation[33], but this result was not agreed upon by another study[34]. In our work,

**682** we found that *MAPT-paRNA* displayed much higher expression in iPSC-derived i3Neurons than

**683** cell lines or other types of iPSC-derived brain cells, and it reached a stable expression in

**684** morphologically mature excitatory neurons (i.e., with more than 5 weeks *in vitro* differentiation).

**685** We considered i3Neurons to be a more relevant model for studying functions of this and other

**686** brain paRNAs. Our knockdown of *MAPT-paRNA* did not impact *MAPT* expression either at

**687** transcriptional or protein levels. This result was also consistent in SH-5YSY, a neuroblastoma

**688** cell line model that displays low levels of *MAPT-paRNA*. In addition to the knockdown results,

**689** the poor correlation between paRNA/mRNA changes in AD also supports that if paRNAs bear

**690** functional roles, they unlikely regulate the genes directly adjacent to them. Furthermore, during

**691** m6A/METTL3 inhibitor treatment (STM2457), while *MAPT-paRNA* expression was reduced,

**692** the neighboring *MAPT* mRNA did not change. Together, our data are in agreement with a

**693** conclusion that *MAPT-paRNA* does not regulate the neighboring *MAPT* expression or translation.

**694**

**695** ***MAPT-paRNA* acts as a global regulator of neuronal/synaptic gene expression and protects**

**696** **neuronal survival**

**697** Instead of regulating the neighboring *MAPT* gene, we found that *MAPT-paRNA* knockdown in

**698** mature i3Neurons altered around 200 genes, including both genes on the same chromosome and

**699** a large majority on other chromosomes. This indicates that *MAPT-paRNA* plays a regulatory role

**700** both *in cis* and *in trans*. By integrative analysis of the target genes and RNA-DNA interactome

**701** data in the human brain offered by the MUSIC dataset[59], we found that the function of *MAPT-*

**702** *paRNA* can be explained by its direct interaction with target genes in the 3D nucleus of

**703** excitatory neurons. Interestingly, from MUSIC as well as snRNA-seq data, m6A-modified

704  paRNAs are more detectable. Also, m6A-modified paRNAs tend to display more target genes

705  and stronger contact strength with their target genes. These together support a positive

706  correlation between m6A and paRNA stability/functionality. In addition to *MAPT-paRNA*, our

707  analysis also found that cell-type-specific paRNAs in neurons often contact important

708  neuronal/synaptic genes. Many AD-deregulated paRNAs in Ex neurons can contact synaptic

709  genes more than background levels. These results indicate that many paRNAs may play roles in

710  cell-type-specific gene regulation in human brains. Distinct from the past work that often found

711  expression of paRNAs positively correlates with[23-26], and in some cases functionally impacts, the

712  expression of the neighboring gene sharing a promoter[27,28], our current findings offer a renewed

713  understanding of paRNAs as global regulators of gene expression *in cis* and *in trans*.

714

715  It is interesting that despite that many paRNAs can contact the same DNA loci (e.g., *MEF2C*),

716  knockdown of a single *MAPT-paRNA* can already cause obvious change of *MEF2C*

717  transcription. We found that in MUSIC data these paRNAs mostly engage with the target DNA

718  alone, i.e., there are rarely any molecular complexes that contain more than one paRNA (data not

719  shown). It is unknown how many of the 31 paRNAs that interact with *MEF2C* loci in Fig. 5H

720  can play a functional role in augmenting *MEF2C* transcription - it could be a few, and some

721  could even suppress *MEF2C* transcription. It is noteworthy that *MAPT-paRNA* may also impact

722  the transcription of these other paRNAs, which we noticed in i3Neurons with *MAPT-paRNA*

723  knockdown. We speculate that the *MAPT-paRNA* inhibition results in a collateral damage to a

724  putative "paRNA network" that could reduce the transcription of *MEF2C* gene from two layers:

725  1), directly from the loss of *MAPT-paRNA*; 2) indirectly from other paRNAs that are affected by

726  *MAPT-paRNA* loss. RNA transcription is being increasingly appreciated to take place in bursts[78].

727  We propose that many paRNAs are produced in dynamic transcriptional bursts, and they act via

728  dynamic interaction with target gene DNAs to achieve transcriptional regulation, potentially in a

729  collaborative manner.

730

731  As *MAPT-paRNA* showed increased expression in AD, we further explored its relevance to AD

732  disease etiology. A glutamate-induced neuronal excitotoxicity assay showed that *MAPT-paRNA*

733  plays a protective role under these conditions, which can be at least partially explained by its

734  positive regulation of key synaptic regulators such as MEF2C and SYNGAP1. Similar protective

735    role of this paRNA was found when neurons were challenged with Aβ-42 directly, one of the

736    most known neuronal stresses in AD. We are tempted to speculate that *MAPT-paRNA* and

737    perhaps some other regulatory paRNAs are upregulated in AD brains to safeguard key

738    synapse/neuronal gene expression so as to rectify the declining neuronal functions. However, the

739    full mechanisms underlying such paRNA regulation in human AD brains remain to be

740    determined at this stage. Future research is warranted to dissect the cause of paRNA deregulation

741    in AD, as well as the detailed mechanisms as to how individual paRNAs can regulate target

742    genes in a 3D nucleus.

743

744    **Limitations of the current study**

745    We utilized six brain samples from NCI and AD donors in this study, which in our knowledge,

746    represented one of the largest that studied total RNA m6A methylome in human brains from

747    normal/AD. However, this number remains limited, and some of the differential m6A sites

748    revealed by current work will need additional larger datasets to be fully validated. Future work

749    may also aim to profile RNA m6A methylome from multiple brain regions and/or from purified

750    individual brain cell types to achieve higher temporal and spatial resolution. In this work we

751    employed the MUSIC data to study RNA-DNA interactomes of paRNAs to understand the

752    mechanisms of their action in gene regulation, but we observed that the detectability of paRNAs

753    in MUSIC[59] is lower than that of snRNA-seq data[52]. For example, about 10-20% of Ex neurons

754    in snRNA-seq can detect *MAPT-paRNA* expression but this number ranges from one to a few

755    percent in MUSIC. Therefore, the target gene numbers and DNA contact strengths of paRNAs

756    seen in MUSIC may represent an under-estimation, and the paRNA-DNA interactome changes

757    in AD cannot be confidently calculated at this stage. In addition, regarding the role of m6A, we

758    noted that the change of *MAPT-paRNA* expression appeared to be quantitative after m6A

759    inhibition (by either chemical or genetic approaches). This suggests that m6A is likely one of the

760    mechanisms, rather than the only, that can impact *MAPT-paRNA* expression in human brains.

761

762    In summary, our results provided a blueprint of the m6A methylome in human brain and AD

763    disease, particularly on various ncRNAs. We reveal previously unknown roles of paRNAs, as

764    exemplified by *MAPT-paRNA,* as global transcriptional regulators in human neurons via

765    navigating 3D nuclear organization, offering new insights into the epitranscriptome regulation of

766    brain gene expression, neuronal survival, and AD pathogenesis.

**Methods**

**Human brain sample collection**

Together with Dr. Hui Zheng (Baylor College of Medicine), we collected RNAs from the middle frontal cortex (FC) of 12 Normal and AD patients (**Supplementary Table 1**). Paired total RNA-seq and m6A RNA methylome (m6A RIP-seq) data were generated from these samples. These tissues were originally collected by the Center for Neurodegenerative Disease Research (CNDR) from University of Pennsylvania and were provided to Dr. Hui Zheng.


**Cell culture**

H1-hESCs (WA01) and WTC11 iPSCs were purchased from WiCell and Coriell, respectively. WTC11-Ngn2 iPSCs with doxycycline-inducible Ngn2 expression cassette was generously provided by Drs. Li Gan[54] and Yin Shen (UCSF). Both iPSCs and ESCs were maintained in mTeSR1 medium (Stemcell Technologies) on Matrigel-coated plates (Corning, 354230) with daily medium replacement. We followed NIH 4D nucleome standard protocol for cell maintenance. HMC3 and SH-SY5Y were purchased from ATCC and were cultured in DMEM/F12 supplemented with 10% fetal bovine serum (FBS).


**Differentiation of H1-hESCs to NPCs and astrocytes**

H1-hESCs derived NPCs and astrocytes were generated according to a previous report[79]. In brief, hESCs were dissociated into single cells and cultured in AggreWell 800 plates (Stemcell Technologies, 34811) to form embryoid bodies (EBs) in Neural Induction Medium (Stemcell Technologies). On day 5, EBs were collected and transferred to 6-well plates coated with Matrigel for culture in the NPC medium. Neural rosettes were collected and dissociated into single cells using Neural Rosette Selection Reagent (StemCell Technologies, 05832) after 14 days of culture. The hESCs-derived NPCs were then cultured in Neural Progenitor Medium (Stemcell Technologies, 05833), and passaged every 4-5 days. Following validation by immunostaining with NPC markers, the cells were cryopreserved in liquid nitrogen for future usage. For the differentiation of NPCs into astrocytes, NPCs were dissociated into single cells using accutase (Thermo Fisher, 00-4555-56) and plated on Matrigel-coated plates in astrocyte medium (ScienCell Research Laboratories, 1801) for 20 days, followed by splitting and

33

797    subculturing until day 75. After validation by immunostaining with astrocyte markers, the cells

798    were frozen for future analysis.

799

800    **Differentiation of WTC11 iPSCs to microglia**

801    iPSC-derived microglia were generated following established protocols with some

802    modifications[80,81]. In brief, iPSCs were cultured in mTeSR plus medium (Stemcell Technologies)

803    on Matrigel-coated plates with daily medium replacement. The cells were dissociated into single

804    cells using accutase and cultured in a 96-well ultra-low attachment plate (Corning, 7201680) to

805    form yolk-sac embryoid bodies (YS-EBs) in 100 µL YS-EBs medium (10 mM ROCK inhibitor,

806    50 ng ml-1 BMP-4, 20 ng ml-1 SCF, and 50 ng ml-1 VEGF-121 in mTeSR plus), with 10,000

807    cells per well on Day 0. The culture medium was replaced on Days 2 and 4 with fresh YS-EBs

808    medium without ROCK inhibitor. On Day 5, the YS-EBs were transferred to a 6-well plate with

809    10-12 YS-EBs per well and incubated in 3 mL hematopoietic medium (2 mM GlutaMax, 100 U

810    ml-1 penicillin, 100 mg ml-1 streptomycin, 55 mM β-mercaptoethanol, 100 ng ml-1 M-CSF, and

811    25 ng ml-1 IL-3 in X-VIVO 15) to induce the generation of primitive macrophage precursors

812    (PMPs). The medium (2 mL) was replaced with fresh hematopoietic medium every 5 days, and

813    PMPs typically emerged as rounded brilliant cells in suspension within 2 weeks. Subsequently,

814    PMPs were harvested from suspension and cultured on Matrigel-coated 6-well plates in

815    microglia medium (DMEM/F12, 2X insulin-transferrin-selenium, 2X B27, 0.5X N2, 1X

816    GlutaMax, 1X non-essential amino acids, 400 µM monothioglycerol, 5 µg ml-1 insulin)

817    supplemented with three protein factors (100 ng ml-1 IL-34, 50 ng ml-1 TGFβ1, and 25 ng ml-1

818    M-CSF) for 25 days, with half-medium replacement every 3 days. After 25 days of culture, the

819    cells were further incubated in microglia medium supplemented with five protein factors (100 ng

820    ml-1 IL-34, 50 ng ml-1 TGFβ1, 25 ng ml-1 M-CSF, 100 ng ml-1 CD200, and 100 ng ml-1

821    CX3CL1) for an additional 3 days to achieve further maturation. Following validation through

822    immunostaining with microglial markers, the iPSC-derived microglia were ready for subsequent

823    treatment or analysis.

824

825    **i3Neuron differentiation**

826    WTC11-Ngn2 iPSCs were utilized to generate i3Neurons following a previously established

827    protocol [52]. For pre-differentiation, WTC11-Ngn2 iPSCs were cultured with 2 µg ml-1

828     doxycycline in knockout DMEM/F12 medium supplemented with 1× N2, 1× NEAA, 1 µg ml−1

829     mouse laminin, 10 ng ml−1 brain-derived neurotrophic factor (BDNF) and 10 ng ml−1 NT3 for

830     three days. ROCK inhibitor (10 µM) was included in the predifferentiation media for the first

831     day, and the medium was replaced daily. During the maturation phase, predifferentiated neural

832     cells were dissociated into single cells using accutase and plated on Poly-L-Ornithine-coated

833     plates in maturation medium containing equal parts DMEM/F12 and Neurobasal-A with

834     2 µg ml−1 doxycycline, 0.5× B-27, 0.5× N-2, 1× NEAA, 0.5× GlutaMax, 1 µg ml−1 mouse

835     laminin, 10 ng ml−1 BDNF and 10 ng ml−1 NT3. Doxycycline was only added to the maturation

836     medium on the first day and omitted thereafter. Half of the medium was replaced weekly for the

837     first 2 weeks, and the medium volume was doubled on week 3. Subsequently, one third of the

838     medium was replaced weekly until 8 weeks for further treatment.

839

840     *MAPT-paRNA* **stability measurement**

841     To study the effect of m6A methylation on *MAPT-paRNA* stability, 8-week-old i3Neurons were

842     treated with m6A/METTL3 inhibitor STM2457 (10 µM, MedChemExpress, HY-134836) or

843     DMSO vehicle for 24 hours. Following this treatment, Flavopiridol (2 µM, Sigma, F3055) was

844     added to inhibit transcriptional activity. The RNA levels of *MAPT-paRNA* were then measured at

845     various time points after transcriptional inhibition using RT-qPCR.

846

847     **Antisense oligonucleotides (ASOs)-based Knockdown**

848     Knockdown experiments were performed using antisense oligonucleotides (ASOs) with

849     modifications by the Affinity Plus nucleic acid modification (IDT) (**see Supplementary Table**

850     **9**). A sequence-scrambled ASO (Scr ASO) was used as a control. ASOs was dissolved in TE

851     buffer (10 mM Tris-HCl, pH 7.4, 1 mM EDTA) and directly added to the i3Neuron culture

852     without any transfection reagent (termed gymnosis) at a final concentration of 10µM. After 3

853     days of ASOs treatment (unless otherwise indicated), cells were harvested for downstream

854     analysis.

855

856     **Western blotting analysis**

857     Cells were washed twice with cold PBS buffer and subsequently lysed in RIPA buffer (50 mM

858     Tris, pH 7.4, 150 mM NaCl, 1 mM EDTA, 0.1% SDS, 1% NP-40, 0.5% sodium deoxycholate)

859    containing cOmplete Mini Protease Inhibitor Cocktail (Roche, 11836153001) on ice for 30

860    minutes. Following centrifugation at 12,000 × g for 10 minutes at 4°C, the supernatants were

861    combined with 2x Laemmli sample buffer (Bio-Rad, 1610737) and boiled at 95 °C for 10

862    minutes. The protein samples were loaded and separated using 4%–15% SDS–PAGE gradient

863    gels, then transferred to a PVDF membrane (Bio-Rad, 1620260). Subsequently, the membranes

864    were blocked in 5% skim milk in TBST (20 mM Tris, 150 mM NaCl, and 0.2% Tween-20, w/v)

865    for 1 hour and incubated with primary antibodies, anti-SYNGAP1 (1:2000; CST; #62193S), anti-

866    MEF2C (1:1000; Abcam; #ab211493), anti-HDAC4 (1:2000; CST; #7628T), anti-Synapsin1

867    (1:1000; SYSY; #106011), anti-PSD95 (1:1000; Sigma; #MAB1596), anti-GluN1 (1:1000;

868    SYSY; #114011), anti-GluA2 (1:1000; BioLegend; #810501), anti-Total Tau (1:20000; Dako;

869    #A0024), anti-pTau (Ser202/Thr205) (1:1000; Thermo Fisher; #MN1020), anti-Tubulin (1:5000;

870    Thermo Fisher; #A11126), or anti-GAPDH (1:50000; Proteintech; #60004). After three washes

871    in TBST, the membranes were incubated with horse-radish peroxidase (HRP)-conjugated

872    secondary antibody for 1 hour. Following six washes, protein bands were visualized using the

873    Enhanced Chemiluminescence kit (Pierce) and developed in the Bio-Rad ChemiDoc gel imaging

874    system. Band intensities were quantified using ImageJ software, with tubulin blots serving as

875    loading controls.

876

**877    Glutamate-induced neuronal excitotoxicity assay**

878    To investigate the neuroprotective role of *MAPT-paRNA*, we implemented glutamate-induced

879    excitotoxicity based on established protocols with slight modifications[74,82]. In detail, i3Neurons

880    were cultured and differentiated in a 24-well plate for 8 weeks and treated with Scr ASO or

881    MAPT-paRNA-ASO1 for 3 days. Subsequently, vehicle or 10µM L-glutamate (Sigma, G1251)

882    was introduced into the medium for 2 hours. Then the cells were stained with Hoechst 33342

883    (5 µg ml−1) (Thermo Fisher, 62249) and propidium iodide (PI, 1 µg ml−1) (Thermo Fisher,

884    P21493) for 30 min to visualize total and dead cells, respectively. Images were captured using a

885    Keyence BZ-X810 Fluorescence Microscope, and neurons from at least 3 wells were quantified.

886    To assess the toxicity of ASOs alone on i3Neurons, the same protocol was applied, excluding the

887    L-glutamate treatment.

**888    Beta-amyloid (Aβ-42)-induced cytotoxicity**

889    To assess the role of MAPT-paRNA under Aβ-induced stress, 8-week-cultured i3Neurons were

890    treated with either Scr ASO or MAPT-paRNA-ASO1 in the presence of scrambled beta-amyloid

891    (Scr Aβ-42, Anaspec, #AS-25382) or beta-amyloid (Aβ-42, Anaspec, #AS-64129-05) for six

892    consecutive days. Cell cytotoxicity was evaluated daily by measuring lactate dehydrogenase

893    (LDH) levels in the culture media using the LDH Assay Kit (Sigma, #MAK066).

894    **Electrophysiological recordings**

895    Electrophysiological recordings were conducted at room temperature using 8-week-cultured

896    i3Neurons in a whole-cell patch-clamp configuration. Patch pipettes with a resistance of 8–15

897    MΩ were filled with an internal solution containing 135 mM CsF, 33 mM CsCl, 2 mM $MgCl_2$, 1

898    mM $CaCl_2$, 11 mM EGTA, and 10 mM HEPES (pH 7.4). The external ACSF solution consisted

899    of 140 mM NaCl, 7 mM KCl, 2 mM $CaCl_2$, 10 mM HEPES, 10 mM glucose, 10 μM bicuculline,

900    and 1 mM TTX (pH 7.4). To selectively study NMDA receptor-mediated currents with

901    glutamate, non-NMDA receptors were blocked using 10 μM NBQX. Conversely, for

902    investigating AMPA receptor-mediated currents, NMDA receptors were blocked with 100 μM

903    APV and 25 μM DCKA. External solutions were locally applied to neurons using an SF-77B

904    Fast-Step perfusion system (Warner Instruments). All recordings were performed at room

905    temperature with a holding potential of −60 mV using an Axopatch 200B amplifier (Molecular

906    Devices). Data were acquired at 10 kHz using pCLAMP10.7 software (Molecular Devices) and

907    filtered online at 5 kHz. Current densities were calculated by dividing the recorded current (pA)

908    by the measured cell membrane capacitance (pF).

909    **Immunocytochemistry**

910    For immunofluorescence immunostaining, the cells were cultured on coverslips, then washed

911    twice with PBS and fixed in cold methanol (-20°C) for 15 min. Subsequently, the cells were

912    permeabilized and blocked with PBS containing 5% goat serum, 5% BSA (bovine serum

913    albumin), and 0.3% Triton X-100 for 1 h, followed by incubation with primary antibodies diluted

914    in blocking buffer overnight at 4°C. After incubation with fluorescence-conjugated secondary

915    antibodies at room temperature for 1 hour, cell nuclei were counterstained with DAPI, and

916    images were acquired using a confocal microscope (Nikon A1) or fluorescence microscope

917    (Keyence). Antibodies used for immunocytochemistry were against PSD95 (1:200; Sigma;

918    #MAB1596), GluN1 (1:200; SYSY; #114011), NeuN (1:200; ThermoFisher; #702022), and

37

919 MAP2 (1:400; Abcam; #ab5392). To quantify the intensity of immunostaining images, ImageJ

920 software (ImageJ website: http://imagej.nih.gov.laneproxy.stanford.edu/ij/) was used. A

921 minimum of 15 neurons from 3 separate experiments were quantified for statistical analysis.

922

**Quantitative RT-PCR (qRT-PCR)**

924 Total cellular RNAs were extracted by TRIzol (Thermo Fisher) or Zymo RNA miniprep kit

925 (Zymo Research), following the respective manufacturer's instructions. The extracted RNA

926 underwent reverse transcription by SuperScript IV (Thermo Fisher) for first strand cDNA

927 synthesis using random hexamer. For qPCR, the SsoAdvanced Universal SYBR green Supermix

928 (Bio-Rad) was used according to the standard parameters recommended by the manufacturer.

929 Primer sequences were shown in **Supplementary Table 9**. All qPCR analyses were performed

930 in triplicate, and each value was denoted by a black dot.

931

**RNA-seq, MeRIP-seq, and MeRIP-qPCR**

933 RNA-seq and MeRIP-seq were performed according to our previous report with some

934 modifications [12]. Total RNA (2-5 μg) was fragmented at 70 °C for 6 min in the fragmentation

935 buffer (10 mM ZnCl2, 10 mM TrisHCl pH7.4), following precipitation the RNA was

936 resuspended with ice-cold IP buffer (10 mM Tris-HCl, pH 7.4, 150 mM NaCl, 0.1% NP-40, 20

937 U/mL Superase-In, 1× Protease Inhibitor) to a final volume of 1050 μL. Of this, 50 μL of diluted

938 RNA was utilized for RNA-seq (5% input for m6A IP) and the remaining 1000 μL was reserved

939 for MeRIP-seq (Methylated RNA immunoprecipitation sequencing). To prepare anti-m6A

940 antibody conjugated beads, 20 μL of Dynabeads Protein G beads (Thermo Fisher) was washed 3

941 times with 1ml IP buffer and then incubated with 1 μg of m6A antibody (Synaptic Systems, #

942 202003) at room temperature for 30min. The conjugated anti-m6A-Dynabeads were washed in

943 1ml IP buffer 3 times. Subsequently, the RNA sample was mixed with the beads and rotated at

944 4 °C for 3 hours. The beads were then washed in the IP buffer 5 times. The immunoprecipitated

945 RNAs were extracted from the beads by TRIzol-LS (Thermo Fisher). The extracted RNA was

946 subjected to the next generation sequencing library preparation for RNA-seq and MeRIP-seq, as

947 well as qPCR, to quantify the m6A levels.

948

**Library Preparation and Sequencing**

950    RNA samples were collected by one of two methods: lysis in TRIzol reagent (Thermo Fisher) for

951    RNA-seq and MeRIP-seq, followed by standard phenol-chloroform extraction methods; or

952    alternatively, lysis was performed using Zymo Research Quick-RNA MiniPrep kit (Genesee

953    Scientific) for regular qPCR following the manufacturer protocol. Libraries for RNA-Seq and

954    MeRIP-Seq were made with NEBNext Ultra II Directional Library Prep Kit for Illumina (NEB,

955    #E7760) following the manufacturer's instructions. Ribosome RNA was depleted with NEBNext

956    rRNA Depletion Kit (NEB, #E6301S). The generated libraries were quantified using the Qubit-3

957    system and/or qPCR. Sequencing of the libraries was performed using a NextSeq 550 platform

958    (Illumina) with paired-end sequencing (40/40nt mode).

959

960    **RNA-seq data analysis**

961    We used FastQC (v.0.11.8) (https://www.bioinformatics.babraham.ac.uk/projects/fastqc/) to

962    check the quality of RNA-seq raw reads. RNA-seq clean reads were aligned to the human

963    reference genome (hg19) or mouse reference genome (m31) from the UCSC database using

964    HISAT2 (v.2.2.1)[83] with *-k 1 --no-discordant --rna-strandness RF*. StringTie (v.2.1.6)[84] was

965    implemented to assemble and quantify transcripts based on gencode.v19.annotation.gtf (human)

966    or gencode.vM31.annotation.gtf (mouse). DESeq2 (v.1.34.0)[85] was run to analyze differentially

967    expressed genes (DEGs). DEGs between AD and Normal groups were defined based on *p.adj* <

968    0.05 and absolute $\log_2$foldchange > 1. Differentially expressed paRNAs between Normal and

969    AD/ALS/PD/FTD brains were selected based on *p.adj* < 0.05 and absolute $\log_2$foldchange >

970    log2(1.5).  For *MAPT-paRNA* control and KD RNA-seq data, DEGs were defined based on *p.adj*

971    < 0.05 and absolute $\log_2$foldchange > log2(1.5).

972

973    **ChIP-seq analysis**

974    We firstly downloaded Non Cognitive Impairment (NCI) and AD H3K27ac and H3K4me3

975    ChIP-seq fastq files from ENCODE (https://www.encodeproject.org/brain-

976    matrix/?type=Experiment&status=released&internal_tags=RushAD) and H3K27ac ChIP-seq

977    data (GSE153875) (Nativio et al. [36]). We used FastQC (v.0.11.8)

978    (https://www.bioinformatics.babraham.ac.uk/projects/fastqc/) to check the quality of ChIP-seq

979    reads. We applied Bowtie2 (v.2.2.5)[86] with --very-sensitive to map clean reads from ChIP-seq to

980    hg19 from the UCSC database, and duplicates are further removed with picard. MACS3

981    (v.3.0.0a6)[39] (https://github.com/macs3-project/MACS) was used to call H3K27ac and

982    H3K4me3 peaks, respectively.

983

984    *De novo transcript calling*

985    We followed the previous method[42,43] to identify RNA transcripts using STAN R package

986    (v.2.22.0)[87]. Briefly, we merged the bam files from the same group to increase the sequencing

987    depth, and convert the bam to bed files. Next, we applied the STAN package to the bed file with

988    default parameters. To define paRNAs, the transcription start sites (TSSs) of any possible

989    paRNAs overlapping with the promoter regions (-2kb to 2kb) of genes were retained.

990

991    **Long-reads Nanopore Direct RNA-seq data Analysis**

992    We downloaded the long-reads RNA-seq datasets from ENCODE

993    (https://www.encodeproject.org/brain-

994    matrix/?type=Experiment&status=released&internal_tags=RushAD). We followed the ENCODE

995    pipeline to reanalyze long-read RNA-seq datasets. Here we used minimap2 (v.2.17-r941)[88] to

996    map the long-read RNA-seq data to the hg19 genome build. Next, TALON (v5.0)[89] was used to

997    quantify the expression of transcripts. Any lincRNA, antisense RNA, processed_transcript or

998    unannotated transcripts overlapping with the transcription start sites (TSSs) of PCGs were

999    retained.

1000

1001    **MeRIP-seq data analysis**

1002    Similar to RNA-seq data analysis, we used the same pipeline to map clean MeRIP-seq data to the

1003    human reference genome. We used MACS3 (v.3.0.0a6)[39] (https://github.com/macs3-

1004    project/MACS) with --nomodel --extsize 100 to call m6A peaks.The high-confidence m6A peaks

1005    were retained based on q value $\leq 10^{-5}$ and fold change $\geq 5$. We used bedtools (v.2.30.0)[90] to get

1006    intersected m6A peaks detected in at least 3 samples. We used ChIPseeker (v.1.40.0)[91] to

1007    annotate the genomic region of a m6A peak as TSS, exon, 5′ UTR, 3′ UTR, intronic or

1008    intergenic. The 'gencode.v19.annotation.gtf' was used as the transcript database. Gene promoter

1009    regions were defined on the basis of -2 kb distance from TSS. For m6A peaks annotated to

1010    ncRNAs, we used m6A peaks to overlap with ncRNAs identified by *de novo* calling or repetitive

1011    elements downloaded from UCSC Genome Browser.

40

**Differential analysis of m6A peaks**

The gained or lost m6A peaks were determined by whether the genomic coordinates of any m6A peaks overlap or not. Of note, this criterion is markedly biased by the peak calling algorithm. For example, the enrichment fold of a genomic region is 4.9 and 5.1 in Normal and AD brains, respectively. Thus, this genomic region would have a m6A peak in AD, but not in Normal brains. Moreover, the difference in m6A ratio (MeRIP/input) in this genomic region between Normal and AD brains was not large. The existing algorithms analyzing differential m6A peaks divided the genomic regions into different bin sizes and compared the differences in m6A ratio between case and control samples. These algorithms have at least 3 limitations. First of all, there is no gold standard for choosing a proper bin size. In addition, continuous bin sizes have significant differences in m6A ratio, these continuous bin sizes would be concatenated, which would make a m6A peak region large. Third, the genomic coordinates of these differential m6A peaks called by the existing algorithms do not match the genomic coordinates of m6A peaks called by MACS3. To address these questions, we merged the m6A peaks from Normal and AD brains to obtain unique m6A peaks, and then calculated the RNA (referred to as *raw FPKM(RNA)*) and m6A methylation (referred to as *raw FPKM(m6A)*) levels for each m6A peak region. Given the sparsity of RNAs in some m6A peak regions, we added a pseudocount of the first quantile of RNA levels from each input sample to *raw FPKM(RNA)* to get the *final FPKM(RNA)*, and calculated the m6A ratio based on the *raw FPKM(m6A)* divided by *the final FPKM(RNA)*. Here is the formula for the normalized m6A ratio:

$\frac{FPKM(MeRIP)}{FPKM(Input)+pseudoCount}$. We further removed the outliers of m6A ratio less than 3.5 based on the quantile distributions of m6A ratio. Next, we performed the paired student's t test for m6A ratio of each m6A peak between AD and Normal brains. We selected the differential m6A peaks based on the fold change > 1.5 and p < 0.1.

**Gene Ontology analysis**

We applied gProfiler2 (v.0.2.2)[92] to analyze the functional enrichment of genes. Significant GO terms will be selected based on a 5% false discovery rate (FDR).

**snRNA-seq data analysis**

41

1042   We downloaded control and Alzheimer's disease snRNA-seq datasets[52]. Based on the previous

1043   method[93], we used the cellranger count (v.7.0.0)[94] with default parameters to align the snRNA-

1044   seq data to the hg19 human reference genome including mRNAs and paRNAs to produce the

1045   raw cell-by-gene count matrix based on the barcode matrix for all snRNA-seq libraries. Next, we

1046   used Seurat (v.5.0.0)[95] to filter out low quality nuclei based on nFeature_RNA > 200 &

1047   nFeature_RNA < 10000 & percent.mt < 5. Subsequently, the merged expression matrix was

1048   normalized by the NormalizeData with default parameters from Seurat. The principal

1049   components were calculated using the first 3000 variable genes, and the Uniform Manifold

1050   Approximation and Projection (UMAP) analysis was performed with RunUMAP from Seurat.

1051   The FindAllMarkers from Seurat was used to analyze the differentially expressed genes across

1052   different clusters. Finally, we used the previously identified marker genes[52] to define the

1053   different cell clusters or cell types. Here if a paRNA was detected in more than 3% cells of a

1054   given cell type, then that paRNA was defined as a detected paRNA in that cell type in snRNA-

1055   seq data.

1056

1057   **MUSIC data analysis**

1058   To analyze how many paRNAs are detected by MUSIC data, we directly used the processed

1059   reads/cells/complex matrix reported in Wen et al.[59], (which is in hg38 genome build). We

1060   liftovered the genomic coordinates of our paRNAs from hg19 genome to hg38, and intersected

1061   the genomic coordinates of paRNAs we identified in human brain bulk RNA-seq datasets with

1062   the RNA reads from MUSIC data. Here if a paRNA was detected in more than 3% cells of a

1063   given cell type based on the cell barcoder (CB), then that paRNA was defined as a detected

1064   paRNA in that cell type in MUSIC data. The expression pattern of paRNAs is similar when

1065   using a more stringent cutoff (e.g., 5% of cells expressing paRNAs). To identify the target genes

1066   of paRNAs of interest, the DNA reads interacting with paRNAs were identified based on shared

1067   cell barcodes and molecular barcodes (CBMB) between RNA reads and DNA reads. To annotate

1068   these DNA reads to genes, we used the gene body to overlap with the DNA reads interacting

1069   with paRNAs. To remove technical issues, we remove large molecular complexes with RNA

1070   reads>50 and DNA reads>1000. We followed the method described by Wen et al.[59] to calculate

1071   the contact strength between RNA reads and DNA reads in a complex: $\frac{M*N}{M+N}$, M and N represent

1072   the number of RNA reads and DNA reads in a complex, respectively. Synaptic genes (n=393)

1073    were extracted from **Supplementary Fig, 11C**, and then we calculated the contact strength

1074    between AD-deregulated paRNAs (DE paRNAs, n = 47) / non-AD-deregulated paRNAs (n =

1075    346) and these synaptic genes (n=393).

1076

1077    **Motif analysis**

1078    We ran Homer (findMotifsGenome -rna -len 5,6,7)[96] to analyze m6A peaks and to identify m6A

1079    motifs.

1080

1081    **Quantification and statistical analysis**

1082    All bar graphs of qPCR data were presented as mean ± SD as indicated in figure legend using

1083    Prism 6.0. Two-tailed Student's t-test was used to compare means between groups as indicated; p

1084    < 0.05 was considered significant, and p values with asterisks are indicated in each figure panel.

1085    ∗, p < 0.05; ∗∗, p < 0.01; ∗∗∗p < 0.001. Statistical details of experiments can be found in the

1086    figure legends. No statistical methods were used to pre-determine sample sizes. For all boxplots,

1087    the central lines represent medians; box limits indicate the 25th and 75th percentiles; and

1088    whiskers extend 1.5 times the interquartile range (IQR) from the 25th and 75th percentiles. For

1089    NGS data analysis, statistical analysis was performed using Python (v.3.8) and R (v.4.3), and is

1090    indicated in the legend of each figure panel.

1091

1110

**Author contributions**

1112    W.L., B.H., and Y.S. conceived the project. B.H. conducted all the dry lab experiments. Y.S. did

1113    most of the wet lab experiments, with help from Y.-T.C., X.Z. and N.D. F.X. generated the

1114    original RNA-Seq and MeRIP-Seq datasets. H.Z. and R.C. acquired human brain tissues and

1115    contributed to i3Neuron work, and D.-F.L. and C.S. helped on neuronal/glial cell differentiation

1116    and culture. X.W. and S.Z. shared and helped with MUSIC data. E.F. and V.J. contributed the

1117    electrophysiology results. W.L., B.H., and Y.S. wrote the manuscript, with inputs from all

1118    authors. These authors contributed equally: Benxia Hu, Yuqiang Shi.

1119

**Corresponding author**

1121    Correspondence to Wenbo Li (Wenbo.Li@uth.tmc.edu).

1122

**Declaration of interests**

1124    The authors declare no competing interests.

1125

**Data availability**

1127    Public data:

1128    H3K4me3 and H3K27ac ChIP-seq, and RNA-seq datasets generated from No Cognitive

1129    Impairment and AD DLPFC are available through (https://www.encodeproject.org/brain-

1130    matrix/?type=Experiment&status=released&internal_tags=RushAD). Old and AD lateral

1131    temporal lobe RNA-seq datasets are available through GSE104704 (Nativio et al., PMID:

1132    32989324), and H3K27ac ChIP-seq data are available through GSE153875 (Nativio et al.,

1133    PMID: 29507413). RNA-seq data generated from the 5xFAD mice brain (right cerebral

1134    hemisphere) are available through https://www.synapse.org/#!Synapse:syn21983020. RNA-seq

44

1135    data generated from the 3xTg-AD mouse mode are available through

1136    https://www.synapse.org/#!Synapse:syn22964719. RNA-seq data generated from the P301S

1137    mouse model are available through GSE226385 (Udeochu et al., PMID: 37095396). RNA-seq

1138    data generated from Parkinson's disease are available through GSE148434 (PD, Lee et al.,

1139    PMID: 37058563), Frontotemporal Dementia are available through GSE116622 (FTD, Conlon et

1140    al., PMID: 30003873), and Amyotrophic lateral sclerosis are available through GSE124439

1141    (ALS, Tam et al., PMID: 31665631). RNA-seq data from iPSC-derived cellular models are

1142    available through GSE102956 (Lin et al., Neuron, PMID:29861287). DLPFC Normal and AD

1143    snRNA-seq data are available through GSE174367 (Morabito et al., PMID:34239132).

1144

1145    Data generated by this work:

1146    Data generated in this study have been deposited to NCBI GEO (GSE266459). The reviewer

1147    token is *mjidasquplmzbcx*. Source Data are provided with this paper (Source Data Files 1,2,3).

1148    Source data and codes in this paper are also available at Zenodo

1149    (https://doi.org/10.5281/zenodo.15019230)[97].

1150

1151    **Code availability**

1152    All custom code used in this work is available in the following github

1153    repository:(https://github.com/BenxiaHu/MAPT-paRNA_in_AD). Genomic tracks are generated

1154    by the HiCPlot NGStrack function (https://github.com/BenxiaHu/HiCPlot).

## Reference

1.  2023 Alzheimer's disease facts and figures. (2023). Alzheimers Dement *19*, 1598-1695. 10.1002/alz.13016.

2.  Knopman, D.S., Amieva, H., Petersen, R.C., Chetelat, G., Holtzman, D.M., Hyman, B.T., Nixon, R.A., and Jones, D.T. (2021). Alzheimer disease. Nat Rev Dis Primers *7*, 33. 10.1038/s41572-021-00269-y.

3.  DeTure, M.A., and Dickson, D.W. (2019). The neuropathological diagnosis of Alzheimer's disease. Mol Neurodegener *14*, 32. 10.1186/s13024-019-0333-5.

4.  Nachtergaele, S., and He, C. (2018). Chemical Modifications in the Life of an mRNA Transcript. Annu Rev Genet *52*, 349-372. 10.1146/annurev-genet-120417-031522.

5.  Zaccara, S., Ries, R.J., and Jaffrey, S.R. (2019). Reading, writing and erasing mRNA methylation. Nat Rev Mol Cell Biol *20*, 608-624. 10.1038/s41580-019-0168-5.

6.  Alarcon, C.R., Goodarzi, H., Lee, H., Liu, X., Tavazoie, S., and Tavazoie, S.F. (2015). HNRNPA2B1 Is a Mediator of m(6)A-Dependent Nuclear RNA Processing Events. Cell *162*, 1299-1308. 10.1016/j.cell.2015.08.011.

7.  Liu, J., Dou, X., Chen, C., Chen, C., Liu, C., Xu, M.M., Zhao, S., Shen, B., Gao, Y., Han, D., and He, C. (2020). N (6)-methyladenosine of chromosome-associated regulatory RNA regulates chromatin state and transcription. Science *367*, 580-586. 10.1126/science.aay6018.

8.  Patil, D.P., Chen, C.K., Pickering, B.F., Chow, A., Jackson, C., Guttman, M., and Jaffrey, S.R. (2016). m(6)A RNA methylation promotes XIST-mediated transcriptional repression. Nature *537*, 369-373. 10.1038/nature19342.

9.  Xiang, Y., Laurent, B., Hsu, C.H., Nachtergaele, S., Lu, Z., Sheng, W., Xu, C., Chen, H., Ouyang, J., Wang, S., et al. (2017). RNA m(6)A methylation regulates the ultraviolet-induced DNA damage response. Nature *543*, 573-576. 10.1038/nature21671.

10. Xu, W., Li, J., He, C., Wen, J., Ma, H., Rong, B., Diao, J., Wang, L., Wang, J., Wu, F., et al. (2021). METTL3 regulates heterochromatin in mouse embryonic stem cells. Nature *591*, 317-321. 10.1038/s41586-021-03210-1.

11. Ruckle, C., Kortel, N., Basilicata, M.F., Busch, A., Zhou, Y., Hoch-Kraft, P., Tretow, K., Kielisch, F., Bertin, M., Pradhan, M., et al. (2023). RNA stability controlled by m(6)A methylation contributes to X-to-autosome dosage compensation in mammals. Nat Struct Mol Biol *30*, 1207-1215. 10.1038/s41594-023-00997-7.

12. Xiong, F., Wang, R., Lee, J.H., Li, S., Chen, S.F., Liao, Z., Hasani, L.A., Nguyen, P.T., Zhu, X., Krakowiak, J., et al. (2021). RNA m(6)A modification orchestrates a LINE-1-host interaction that facilitates retrotransposition and contributes to long gene vulnerability. Cell Res *31*, 861-885. 10.1038/s41422-021-00515-8.

13. Liu, J., Gao, M., He, J., Wu, K., Lin, S., Jin, L., Chen, Y., Liu, H., Shi, J., Wang, X., et al. (2021). The RNA m(6)A reader YTHDC1 silences retrotransposons and guards ES cell identity. Nature *591*, 322-326. 10.1038/s41586-021-03313-9.

14. Chelmicki, T., Roger, E., Teissandier, A., Dura, M., Bonneville, L., Rucli, S., Dossin, F., Fouassier, C., Lameiras, S., and Bourc'his, D. (2021). m(6)A RNA methylation regulates the fate of endogenous retroviruses. Nature *591*, 312-316. 10.1038/s41586-020-03135-1.

15. Lee, J.H., Wang, R., Xiong, F., Krakowiak, J., Liao, Z., Nguyen, P.T., Moroz-Omori, E.V., Shao, J., Zhu, X., Bolt, M.J., et al. (2021). Enhancer RNA m6A methylation facilitates transcriptional condensate formation and gene activation. Mol Cell *81*, 3368-3385 e3369. 10.1016/j.molcel.2021.07.024.

1201  16.    Liu, J., Li, K., Cai, J., Zhang, M., Zhang, X., Xiong, X., Meng, H., Xu, X., Huang, Z.,
1202          Peng, J., et al. (2020). Landscape and Regulation of m(6)A and m(6)Am Methylome
1203          across Human and Mouse Tissues. Mol Cell *77*, 426-440 e426.
1204          10.1016/j.molcel.2019.09.032.
1205  17.    Yoon, K.J., Ringeling, F.R., Vissers, C., Jacob, F., Pokrass, M., Jimenez-Cyrus, D., Su,
1206          Y., Kim, N.S., Zhu, Y., Zheng, L., et al. (2017). Temporal Control of Mammalian
1207          Cortical Neurogenesis by m(6)A Methylation. Cell *171*, 877-889 e817.
1208          10.1016/j.cell.2017.09.003.
1209  18.    Shi, H., Zhang, X., Weng, Y.L., Lu, Z., Liu, Y., Lu, Z., Li, J., Hao, P., Zhang, Y., Zhang,
1210          F., et al. (2018). m(6)A facilitates hippocampus-dependent learning and memory through
1211          YTHDF1. Nature *563*, 249-253. 10.1038/s41586-018-0666-1.
1212  19.    Castro-Hernandez, R., Berulava, T., Metelova, M., Epple, R., Pena Centeno, T., Richter,
1213          J., Kaurani, L., Pradhan, R., Sakib, M.S., Burkhardt, S., et al. (2023). Conserved
1214          reduction of m(6)A RNA modifications during aging and neurodegeneration is linked to
1215          changes in synaptic transcripts. Proc Natl Acad Sci U S A *120*, e2204933120.
1216          10.1073/pnas.2204933120.
1217  20.    Djebali, S., Davis, C.A., Merkel, A., Dobin, A., Lassmann, T., Mortazavi, A., Tanzer, A.,
1218          Lagarde, J., Lin, W., Schlesinger, F., et al. (2012). Landscape of transcription in human
1219          cells. Nature *489*, 101-108. 10.1038/nature11233.
1220  21.    Mattick, J.S., Amaral, P.P., Carninci, P., Carpenter, S., Chang, H.Y., Chen, L.L., Chen,
1221          R., Dean, C., Dinger, M.E., Fitzgerald, K.A., et al. (2023). Long non-coding RNAs:
1222          definitions, functions, challenges and recommendations. Nat Rev Mol Cell Biol *24*, 430-
1223          447. 10.1038/s41580-022-00566-8.
1224  22.    Sigova, A.A., Mullen, A.C., Molinie, B., Gupta, S., Orlando, D.A., Guenther, M.G.,
1225          Almada, A.E., Lin, C., Sharp, P.A., Giallourakis, C.C., and Young, R.A. (2013).
1226          Divergent transcription of long noncoding RNA/mRNA gene pairs in embryonic stem
1227          cells. Proc Natl Acad Sci U S A *110*, 2876-2881. 10.1073/pnas.1221904110.
1228  23.    Seila, A.C., Calabrese, J.M., Levine, S.S., Yeo, G.W., Rahl, P.B., Flynn, R.A., Young,
1229          R.A., and Sharp, P.A. (2008). Divergent transcription from active promoters. Science
1230          *322*, 1849-1851. 10.1126/science.1162253.
1231  24.    Core, L.J., Waterfall, J.J., and Lis, J.T. (2008). Nascent RNA sequencing reveals
1232          widespread pausing and divergent initiation at human promoters. Science *322*, 1845-
1233          1848. 10.1126/science.1162228.
1234  25.    Preker, P., Nielsen, J., Kammler, S., Lykke-Andersen, S., Christensen, M.S., Mapendano,
1235          C.K., Schierup, M.H., and Jensen, T.H. (2008). RNA exosome depletion reveals
1236          transcription upstream of active human promoters. Science *322*, 1851-1854.
1237          10.1126/science.1164096.
1238  26.    He, Y., Vogelstein, B., Velculescu, V.E., Papadopoulos, N., and Kinzler, K.W. (2008).
1239          The antisense transcriptomes of human cells. Science *322*, 1855-1857.
1240          10.1126/science.1163853.
1241  27.    Yang, F. (2022). Promoter antisense RNAs: beyond transcription by-products of active
1242          promoters. RNA Biol *19*, 533-540. 10.1080/15476286.2022.2062177.
1243  28.    Yang, F., Tanasa, B., Micheletti, R., Ohgi, K.A., Aggarwal, A.K., and Rosenfeld, M.G.
1244          (2021). Shape of promoter antisense RNAs regulates ligand-induced transcription
1245          activation. Nature *595*, 444-449. 10.1038/s41586-021-03589-x.

1246    29.    Salta, E., and De Strooper, B. (2017). Noncoding RNAs in neurodegeneration. Nat Rev
1247           Neurosci *18*, 627-640. 10.1038/nrn.2017.90.
1248    30.    Idda, M.L., Munk, R., Abdelmohsen, K., and Gorospe, M. (2018). Noncoding RNAs in
1249           Alzheimer's disease. Wiley Interdiscip Rev RNA *9*. 10.1002/wrna.1463.
1250    31.    Rybak-Wolf, A., and Plass, M. (2021). RNA Dynamics in Alzheimer's Disease.
1251           Molecules *26*. 10.3390/molecules26175113.
1252    32.    Faghihi, M.A., Modarresi, F., Khalil, A.M., Wood, D.E., Sahagan, B.G., Morgan, T.E.,
1253           Finch, C.E., St Laurent, G., 3rd, Kenny, P.J., and Wahlestedt, C. (2008). Expression of a
1254           noncoding RNA is elevated in Alzheimer's disease and drives rapid feed-forward
1255           regulation of beta-secretase. Nat Med *14*, 723-730. 10.1038/nm1784.
1256    33.    Simone, R., Javad, F., Emmett, W., Wilkins, O.G., Almeida, F.L., Barahona-Torres, N.,
1257           Zareba-Paslawska, J., Ehteramyan, M., Zuccotti, P., Modelska, A., et al. (2021). MIR-
1258           NATs repress MAPT translation and aid proteostasis in neurodegeneration. Nature *594*,
1259           117-123. 10.1038/s41586-021-03556-6.
1260    34.    Policarpo, R., Wolfs, L., Martínez-Montero, S., Vandermeulen, L., Royaux, I., Peer,
1261           G.V., Mestdagh, P., Sierksma, A., Strooper, B.D., and d'Ydewalle, C. (2023). The MIR-
1262           NAT MAPT-AS1 does not regulate Tau expression in human neurons. bioRxiv,
1263           2023.2001.2027.525631. 10.1101/2023.01.27.525631.
1264    35.    Jobson, D.D., Hase, Y., Clarkson, A.N., and Kalaria, R.N. (2021). The role of the medial
1265           prefrontal cortex in cognition, ageing and dementia. Brain Commun *3*, fcab125.
1266           10.1093/braincomms/fcab125.
1267    36.    Nativio, R., Lan, Y., Donahue, G., Sidoli, S., Berson, A., Srinivasan, A.R.,
1268           Shcherbakova, O., Amlie-Wolf, A., Nie, J., Cui, X., et al. (2020). An integrated multi-
1269           omics approach identifies epigenetic alterations associated with Alzheimer's disease. Nat
1270           Genet *52*, 1024-1035. 10.1038/s41588-020-0696-0.
1271    37.    Subramanian, J., Savage, J.C., and Tremblay, M.E. (2020). Synaptic Loss in Alzheimer's
1272           Disease: Mechanistic Insights Provided by Two-Photon in vivo Imaging of Transgenic
1273           Mouse Models. Front Cell Neurosci *14*, 592607. 10.3389/fncel.2020.592607.
1274    38.    Mathys, H., Peng, Z., Boix, C.A., Victor, M.B., Leary, N., Babu, S., Abdelhady, G.,
1275           Jiang, X., Ng, A.P., Ghafari, K., et al. (2023). Single-cell atlas reveals correlates of high
1276           cognitive function, dementia, and resilience to Alzheimer's disease pathology. Cell *186*,
1277           4365-4385 e4327. 10.1016/j.cell.2023.08.039.
1278    39.    Zhang, Y., Liu, T., Meyer, C.A., Eeckhoute, J., Johnson, D.S., Bernstein, B.E., Nusbaum,
1279           C., Myers, R.M., Brown, M., Li, W., and Liu, X.S. (2008). Model-based analysis of
1280           ChIP-Seq (MACS). Genome Biol *9*, R137. 10.1186/gb-2008-9-9-r137.
1281    40.    Xiong, X., Hou, L., Park, Y.P., Molinie, B., Consortium, G.T., Gregory, R.I., and Kellis,
1282           M. (2021). Genetic drivers of m(6)A methylation in human brain, lung, heart and muscle.
1283           Nat Genet *53*, 1156-1165. 10.1038/s41588-021-00890-3.
1284    41.    Porman, A.M., Roberts, J.T., Duncan, E.D., Chrupcala, M.L., Levine, A.A., Kennedy,
1285           M.A., Williams, M.M., Richer, J.K., and Johnson, A.M. (2022). A single N6-
1286           methyladenosine site regulates lncRNA HOTAIR function in breast cancer cells. PLoS
1287           Biol *20*, e3001885. 10.1371/journal.pbio.3001885.
1288    42.    Schwalb, B., Michel, M., Zacher, B., Fruhauf, K., Demel, C., Tresch, A., Gagneur, J., and
1289           Cramer, P. (2016). TT-seq maps the human transient transcriptome. Science *352*, 1225-
1290           1228. 10.1126/science.aad9841.

43. Shao, R., Kumar, B., Lidschreiber, K., Lidschreiber, M., Cramer, P., and Elsasser, S.J. (2022). Distinct transcription kinetics of pluripotent cell states. Mol Syst Biol *18*, e10407. 10.15252/msb.202110407.

44. Murakami, S., and Jaffrey, S.R. (2022). Hidden codes in mRNA: Control of gene expression by m(6)A. Mol Cell *82*, 2236-2251. 10.1016/j.molcel.2022.05.029.

45. Oakley, H., Cole, S.L., Logan, S., Maus, E., Shao, P., Craft, J., Guillozet-Bongaarts, A., Ohno, M., Disterhoft, J., Van Eldik, L., et al. (2006). Intraneuronal beta-amyloid aggregates, neurodegeneration, and neuron loss in transgenic mice with five familial Alzheimer's disease mutations: potential factors in amyloid plaque formation. J Neurosci *26*, 10129-10140. 10.1523/JNEUROSCI.1202-06.2006.

46. Oddo, S., Caccamo, A., Shepherd, J.D., Murphy, M.P., Golde, T.E., Kayed, R., Metherate, R., Mattson, M.P., Akbari, Y., and LaFerla, F.M. (2003). Triple-transgenic model of Alzheimer's disease with plaques and tangles: intracellular Abeta and synaptic dysfunction. Neuron *39*, 409-421. 10.1016/s0896-6273(03)00434-3.

47. Udeochu, J.C., Amin, S., Huang, Y., Fan, L., Torres, E.R.S., Carling, G.K., Liu, B., McGurran, H., Coronas-Samano, G., Kauwe, G., et al. (2023). Tau activation of microglial cGAS-IFN reduces MEF2C-mediated cognitive resilience. Nat Neurosci *26*, 737-750. 10.1038/s41593-023-01315-6.

48. Oblak, A.L., Lin, P.B., Kotredes, K.P., Pandey, R.S., Garceau, D., Williams, H.M., Uyar, A., O'Rourke, R., O'Rourke, S., Ingraham, C., et al. (2021). Comprehensive Evaluation of the 5XFAD Mouse Model for Preclinical Testing Applications: A MODEL-AD Study. Front Aging Neurosci *13*, 713726. 10.3389/fnagi.2021.713726.

49. Lee, A.J., Kim, C., Park, S., Joo, J., Choi, B., Yang, D., Jun, K., Eom, J., Lee, S.J., Chung, S.J., et al. (2023). Characterization of altered molecular mechanisms in Parkinson's disease through cell type-resolved multiomics analyses. Sci Adv *9*, eabo2467. 10.1126/sciadv.abo2467.

50. Conlon, E.G., Fagegaltier, D., Agius, P., Davis-Porada, J., Gregory, J., Hubbard, I., Kang, K., Kim, D., New York Genome Center, A.L.S.C., Phatnani, H., et al. (2018). Unexpected similarities between C9ORF72 and sporadic forms of ALS/FTD suggest a common disease mechanism. Elife *7*. 10.7554/eLife.37754.

51. Tam, O.H., Rozhkov, N.V., Shaw, R., Kim, D., Hubbard, I., Fennessey, S., Propp, N., Consortium, N.A., Fagegaltier, D., Harris, B.T., et al. (2019). Postmortem Cortex Samples Identify Distinct Molecular Subtypes of ALS: Retrotransposon Activation, Oxidative Stress, and Activated Glia. Cell Rep *29*, 1164-1177 e1165. 10.1016/j.celrep.2019.09.066.

52. Morabito, S., Miyoshi, E., Michael, N., Shahin, S., Martini, A.C., Head, E., Silva, J., Leavy, K., Perez-Rosendahl, M., and Swarup, V. (2021). Single-nucleus chromatin accessibility and transcriptomic characterization of Alzheimer's disease. Nat Genet *53*, 1143-1155. 10.1038/s41588-021-00894-z.

53. Lin, Y.T., Seo, J., Gao, F., Feldman, H.M., Wen, H.L., Penney, J., Cam, H.P., Gjoneska, E., Raja, W.K., Cheng, J., et al. (2018). APOE4 Causes Widespread Molecular and Cellular Alterations Associated with Alzheimer's Disease Phenotypes in Human iPSC-Derived Brain Cell Types. Neuron *98*, 1141-1154 e1147. 10.1016/j.neuron.2018.05.008.

54. Wang, C., Ward, M.E., Chen, R., Liu, K., Tracy, T.E., Chen, X., Xie, M., Sohn, P.D., Ludwig, C., Meyer-Franke, A., et al. (2017). Scalable Production of iPSC-Derived

49

Human Neurons to Identify Tau-Lowering Compounds by High-Content Screening. Stem Cell Reports *9*, 1221-1233. 10.1016/j.stemcr.2017.08.019.

55. Yankova, E., Blackaby, W., Albertella, M., Rak, J., De Braekeleer, E., Tsagkogeorga, G., Pilka, E.S., Aspris, D., Leggate, D., Hendrick, A.G., et al. (2021). Small-molecule inhibition of METTL3 as a strategy against myeloid leukaemia. Nature *593*, 597-601. 10.1038/s41586-021-03536-w.

56. Yang, R., Feng, X., Arias-Cavieres, A., Mitchell, R.M., Polo, A., Hu, K., Zhong, R., Qi, C., Zhang, R.S., Westneat, N., et al. (2023). Upregulation of SYNGAP1 expression in mice and human neurons by redirecting alternative splicing. Neuron *111*, 1637-1650 e1635. 10.1016/j.neuron.2023.02.021.

57. Harrington, A.J., Raissi, A., Rajkovich, K., Berto, S., Kumar, J., Molinaro, G., Raduazzo, J., Guo, Y., Loerwald, K., Konopka, G., et al. (2016). MEF2C regulates cortical inhibitory and excitatory synapses and behaviors relevant to neurodevelopmental disorders. Elife *5*. 10.7554/eLife.20059.

58. Kim, M.S., Akhtar, M.W., Adachi, M., Mahgoub, M., Bassel-Duby, R., Kavalali, E.T., Olson, E.N., and Monteggia, L.M. (2012). An essential role for histone deacetylase 4 in synaptic plasticity and memory formation. J Neurosci *32*, 10879-10886. 10.1523/JNEUROSCI.2089-12.2012.

59. Wen, X., Luo, Z., Zhao, W., Calandrelli, R., Nguyen, T.C., Wan, X., Charles Richard, J.L., and Zhong, S. (2024). Single-cell multiplex chromatin and RNA interactions in ageing human brain. Nature *628*, 648-656. 10.1038/s41586-024-07239-w.

60. Barker, S.J., Raju, R.M., Milman, N.E.P., Wang, J., Davila-Velderrain, J., Gunter-Rahman, F., Parro, C.C., Bozzelli, P.L., Abdurrob, F., Abdelaal, K., et al. (2021). MEF2 is a key regulator of cognitive potential and confers resilience to neurodegeneration. Sci Transl Med *13*, eabd7695. 10.1126/scitranslmed.abd7695.

61. Targa Dias Anastacio, H., Matosin, N., and Ooi, L. (2022). Neuronal hyperexcitability in Alzheimer's disease: what are the drivers behind this aberrant phenotype? Transl Psychiatry *12*, 257. 10.1038/s41398-022-02024-7.

62. Wang, R., and Reddy, P.H. (2017). Role of Glutamate and NMDA Receptors in Alzheimer's Disease. J Alzheimers Dis *57*, 1041-1048. 10.3233/JAD-160763.

63. Kim, J.H., Lee, H.K., Takamiya, K., and Huganir, R.L. (2003). The role of synaptic GTPase-activating protein in neuronal development and synaptic plasticity. J Neurosci *23*, 1119-1124. 10.1523/JNEUROSCI.23-04-01119.2003.

64. Komiyama, N.H., Watabe, A.M., Carlisle, H.J., Porter, K., Charlesworth, P., Monti, J., Strathdee, D.J., O'Carroll, C.M., Martin, S.J., Morris, R.G., et al. (2002). SynGAP regulates ERK/MAPK signaling, synaptic plasticity, and learning in the complex with postsynaptic density 95 and NMDA receptor. J Neurosci *22*, 9721-9732. 10.1523/JNEUROSCI.22-22-09721.2002.

65. Okamoto, S., Li, Z., Ju, C., Scholzke, M.N., Mathews, E., Cui, J., Salvesen, G.S., Bossy-Wetzel, E., and Lipton, S.A. (2002). Dominant-interfering forms of MEF2 generated by caspase cleavage contribute to NMDA-induced neuronal apoptosis. Proc Natl Acad Sci U S A *99*, 3974-3979. 10.1073/pnas.022036399.

66. Barbosa, A.C., Kim, M.S., Ertunc, M., Adachi, M., Nelson, E.D., McAnally, J., Richardson, J.A., Kavalali, E.T., Monteggia, L.M., Bassel-Duby, R., and Olson, E.N. (2008). MEF2C, a transcription factor that facilitates learning and memory by negative

regulation of synapse numbers and function. Proc Natl Acad Sci U S A *105*, 9391-9396. 10.1073/pnas.0802679105.

67. Fenton, T.A., Haouchine, O.Y., Hallam, E.L., Smith, E.M., Jackson, K.C., Rahbarian, D., Canales, C., Adhikari, A., Nord, A.S., Ben-Shalom, R., and Silverman, J.L. (2023). Hyperexcitability and translational phenotypes in a preclinical model of SYNGAP1 mutations. bioRxiv. 10.1101/2023.07.24.550093.

68. Miyamoto, T., Stein, L., Thomas, R., Djukic, B., Taneja, P., Knox, J., Vossel, K., and Mucke, L. (2017). Phosphorylation of tau at Y18, but not tau-fyn binding, is required for tau to modulate NMDA receptor-dependent excitotoxicity in primary neuronal culture. Mol Neurodegener *12*, 41. 10.1186/s13024-017-0176-x.

69. Talantova, M., Sanz-Blasco, S., Zhang, X., Xia, P., Akhtar, M.W., Okamoto, S., Dziewczapolski, G., Nakamura, T., Cao, G., Pratt, A.E., et al. (2013). Abeta induces astrocytic glutamate release, extrasynaptic NMDA receptor activation, and synaptic loss. Proc Natl Acad Sci U S A *110*, E2518-2527. 10.1073/pnas.1306832110.

70. Zeng, M., Shang, Y., Araki, Y., Guo, T., Huganir, R.L., and Zhang, M. (2016). Phase Transition in Postsynaptic Densities Underlies Formation of Synaptic Complexes and Synaptic Plasticity. Cell *166*, 1163-1175 e1112. 10.1016/j.cell.2016.07.008.

71. Tsai, N.P., Wilkerson, J.R., Guo, W., Maksimova, M.A., DeMartino, G.N., Cowan, C.W., and Huber, K.M. (2012). Multiple autism-linked genes mediate synapse elimination via proteasomal degradation of a synaptic scaffold PSD-95. Cell *151*, 1581-1594. 10.1016/j.cell.2012.11.040.

72. Minkeviciene, R., Rheims, S., Dobszay, M.B., Zilberter, M., Hartikainen, J., Fulop, L., Penke, B., Zilberter, Y., Harkany, T., Pitkanen, A., and Tanila, H. (2009). Amyloid beta-induced neuronal hyperexcitability triggers progressive epilepsy. J Neurosci *29*, 3453-3462. 10.1523/JNEUROSCI.5215-08.2009.

73. Zott, B., Simon, M.M., Hong, W., Unger, F., Chen-Engerer, H.J., Frosch, M.P., Sakmann, B., Walsh, D.M., and Konnerth, A. (2019). A vicious cycle of beta amyloid-dependent neuronal hyperactivation. Science *365*, 559-565. 10.1126/science.aay0198.

74. Li, Y., Dou, X., Liu, J., Xiao, Y., Zhang, Z., Hayes, L., Wu, R., Fu, X., Ye, Y., Yang, B., et al. (2023). Globally reduced N(6)-methyladenosine (m(6)A) in C9ORF72-ALS/FTD dysregulates RNA metabolism and contributes to neurodegeneration. Nat Neurosci *26*, 1328-1338. 10.1038/s41593-023-01374-9.

75. Congdon, E.E., Ji, C., Tetlow, A.M., Jiang, Y., and Sigurdsson, E.M. (2023). Tau-targeting therapies for Alzheimer disease: current status and future directions. Nat Rev Neurol *19*, 715-736. 10.1038/s41582-023-00883-2.

76. Jun, G., Ibrahim-Verbaas, C.A., Vronskaya, M., Lambert, J.C., Chung, J., Naj, A.C., Kunkle, B.W., Wang, L.S., Bis, J.C., Bellenguez, C., et al. (2016). A novel Alzheimer disease locus located near the gene encoding tau protein. Mol Psychiatry *21*, 108-117. 10.1038/mp.2015.23.

77. Bellenguez, C., Kucukali, F., Jansen, I.E., Kleineidam, L., Moreno-Grau, S., Amin, N., Naj, A.C., Campos-Martin, R., Grenier-Boley, B., Andrade, V., et al. (2022). New insights into the genetic etiology of Alzheimer's disease and related dementias. Nat Genet *54*, 412-436. 10.1038/s41588-022-01024-z.

78. Rodriguez, J., Ren, G., Day, C.R., Zhao, K., Chow, C.C., and Larson, D.R. (2019). Intrinsic Dynamics of a Human Gene Reveal the Basis of Expression Heterogeneity. Cell *176*, 213-226 e218. 10.1016/j.cell.2018.11.026.

79.  Xu, A., Liu, M., Huang, M.F., Zhang, Y., Hu, R., Gingold, J.A., Liu, Y., Zhu, D., Chien, C.S., Wang, W.C., et al. (2023). Rewired m(6)A epitranscriptomic networks link mutant p53 to neoplastic transformation. Nat Commun *14*, 1694. 10.1038/s41467-023-37398-9.

80.  McQuade, A., Coburn, M., Tu, C.H., Hasselmann, J., Davtyan, H., and Blurton-Jones, M. (2018). Development and validation of a simplified method to generate human microglia from pluripotent stem cells. Mol Neurodegener *13*, 67. 10.1186/s13024-018-0297-x.

81.  Brownjohn, P.W., Smith, J., Solanki, R., Lohmann, E., Houlden, H., Hardy, J., Dietmann, S., and Livesey, F.J. (2018). Functional Studies of Missense TREM2 Mutations in Human Stem Cell-Derived Microglia. Stem Cell Reports *10*, 1294-1307. 10.1016/j.stemcr.2018.03.003.

82.  Zaepfel, B.L., Zhang, Z., Maulding, K., Coyne, A.N., Cheng, W., Hayes, L.R., Lloyd, T.E., Sun, S., and Rothstein, J.D. (2021). UPF1 reduces C9orf72 HRE-induced neurotoxicity in the absence of nonsense-mediated decay dysfunction. Cell Rep *34*, 108925. 10.1016/j.celrep.2021.108925.

83.  Kim, D., Paggi, J.M., Park, C., Bennett, C., and Salzberg, S.L. (2019). Graph-based genome alignment and genotyping with HISAT2 and HISAT-genotype. Nat Biotechnol *37*, 907-915. 10.1038/s41587-019-0201-4.

84.  Pertea, M., Pertea, G.M., Antonescu, C.M., Chang, T.C., Mendell, J.T., and Salzberg, S.L. (2015). StringTie enables improved reconstruction of a transcriptome from RNA-seq reads. Nat Biotechnol *33*, 290-295. 10.1038/nbt.3122.

85.  Love, M.I., Huber, W., and Anders, S. (2014). Moderated estimation of fold change and dispersion for RNA-seq data with DESeq2. Genome Biol *15*, 550. 10.1186/s13059-014-0550-8.

86.  Langmead, B., and Salzberg, S.L. (2012). Fast gapped-read alignment with Bowtie 2. Nat Methods *9*, 357-359. 10.1038/nmeth.1923.

87.  Zacher, B., Lidschreiber, M., Cramer, P., Gagneur, J., and Tresch, A. (2014). Annotation of genomics data using bidirectional hidden Markov models unveils variations in Pol II transcription cycle. Mol Syst Biol *10*, 768. 10.15252/msb.20145654.

88.  Li, H. (2018). Minimap2: pairwise alignment for nucleotide sequences. Bioinformatics *34*, 3094-3100. 10.1093/bioinformatics/bty191.

89.  Wyman, D., Balderrama-Gutierrez, G., Reese, F., Jiang, S., Rahmanian, S., Forner, S., Matheos, D., Zeng, W., Williams, B., Trout, D., et al. (2020). A technology-agnostic long-read analysis pipeline for transcriptome discovery and quantification. bioRxiv, 672931. 10.1101/672931.

90.  Quinlan, A.R., and Hall, I.M. (2010). BEDTools: a flexible suite of utilities for comparing genomic features. Bioinformatics *26*, 841-842. 10.1093/bioinformatics/btq033.

91.  Yu, G., Wang, L.G., and He, Q.Y. (2015). ChIPseeker: an R/Bioconductor package for ChIP peak annotation, comparison and visualization. Bioinformatics *31*, 2382-2383. 10.1093/bioinformatics/btv145.

92.  Kolberg, L., Raudvere, U., Kuzmin, I., Vilo, J., and Peterson, H. (2020). gprofiler2 -- an R package for gene list functional enrichment analysis and namespace conversion toolset g:Profiler. F1000Res *9*. 10.12688/f1000research.24956.2.

93.  Hu, B., Zhuang, X.L., Zhou, L., Zhang, G., Cooper, D.N., and Wu, D.D. (2024). Deciphering the Role of Rapidly Evolving Conserved Elements in Primate Brain

1472 Development and Exploring Their Potential Involvement in Alzheimer's Disease. Mol
1473 Biol Evol *41*. 10.1093/molbev/msae001.
1474 94. Danielski, K. (2023). Guidance on Processing the 10x Genomics Single Cell Gene
1475 Expression Assay. Methods Mol Biol *2584*, 1-28. 10.1007/978-1-0716-2756-3_1.
1476 95. Hao, Y., Stuart, T., Kowalski, M.H., Choudhary, S., Hoffman, P., Hartman, A.,
1477 Srivastava, A., Molla, G., Madad, S., Fernandez-Granda, C., and Satija, R. (2024).
1478 Dictionary learning for integrative, multimodal and scalable single-cell analysis. Nat
1479 Biotechnol *42*, 293-304. 10.1038/s41587-023-01767-y.
1480 96. Heinz, S., Benner, C., Spann, N., Bertolino, E., Lin, Y.C., Laslo, P., Cheng, J.X., Murre,
1481 C., Singh, H., and Glass, C.K. (2010). Simple combinations of lineage-determining
1482 transcription factors prime cis-regulatory elements required for macrophage and B cell
1483 identities. Mol Cell *38*, 576-589. 10.1016/j.molcel.2010.05.004.
1484 97. Hu, B. (2025). MAPT-paRNA in AD. Zenodo. https://doi.org/10.5281/zenodo.15019230.
1485